Three little pieces for computer and relativity

Luciano Rezzolla

Abstract Numerical relativity has made big strides over the last decade. A number of problems that have plagued the field for years have now been mostly solved. This progress has transformed numerical relativity into a powerful tool to explore fundamental problems in physics and astrophysics, and I present here three representative examples. These "three little pieces" reflect a personal choice and describe work that I am particularly familiar with. However, many more examples could be made.

1 Introduction

Numerical relativity has hardly seen better times before. Over the last few years, in fact, a truly remarkable development has shaken the field. Starting from the first simulations showing that black-hole binaries could be evolved for a few orbits [1, 2, 3], or that black-hole formation could be followed stably using simple gauges and without excision [4], new results, some awaited for decades, have been obtained steadily. As a direct consequence of this "Renaissance", it is now possible to simulate binary black holes [5] and binary neutron stars [6] accurately for dozens of orbits, from the weak-field inspiral, down to the final black-hole ringdown (see also [7, 8] for recent reviews).

There are several reasons behind this rapid progress. These include the use of more advanced and accurate numerical techniques [9, 10], the availability of larger computational facilities, but also the development of formulations of the Einstein equations and gauges that are particularly well-suited for numerical evolutions [11, 12, 13, 14, 15, 16, 17, 18, 19, 20, 21]. The phase transition that has taken during this year has radically changed numerical relativity, freeing it from the corner of idealised investigations. Most importantly, it has transformed numerical relativ-

Luciano Rezzolla
Max-Planck-Institut für Gravitationsphysik, Albert-Einstein-Institut, Potsdam, Germany; Institut für Theoretische Physik, Frankfurt am Main, Germany.

ity into a research area where long-standing problems can found a quantitative and accurate solution, and into a tool by means of which it is possible to *explore* fundamental aspects of physics and astrophysics.

Numerous examples could be given to testify this transformation, although I will report here only those that I am particular familiar with. More specifically, in what follows I will discuss: *(i)* how numerical simulations of magnetised neutron stars provide convincing evidence that this process leads to the conditions that are expected behind the phenomenology of short gamma ray burst; *(ii)* how numerical simulations of the head-on collision of selfgravitating fluids boosted at relativistic speeds can be used to understand the conditions leading to the formation of a black hole and provide a dynamical version of the hoop conjecture; *(iii)* how the study of the local properties of apparent horizons can be used to explain bizarre behaviours in binary black-hole simulations and can be effectively correlated with a portion of the spacetime infinitely far away: $\mathscr{J}^+$. This selection is by no means comprehensive, but rather a very personal one, and I apologise in advance for not discussing all the excellent work that cannot find space in this contribution.

2 First piece: From neutrons star to gamma-ray bursts

The numerical investigation of the inspiral and merger of binary neutron stars in full general relativity has seen enormous progress made in recent years. Crucial improvements in the formulation of the equations and numerical methods, along with increased computational resources, have extended the scope of early simulations. These developments have made it possible to compute the full evolution, from large binary-separations up to black-hole formation, without and with magnetic fields [22, 6, 23, 24, 25, 26], and with idealised or realistic equations-of-state [27, 28]. This tremendous advancement is also providing information about the entire gravitational waveform, from the early inspiral up to the ringing of the black hole (see, *e.g.,* [29, 30, 31]). Advanced interferometric detectors starting from 2014 are expected to observe these sources at a rate of $\sim 40-400$ events per year [32].

These simulations also probe whether the end-product of mergers can serve as the "central engine" of short gamma-ray bursts (SGRBs) [33, 34, 35]. The prevalent scenario invoked to explain SGRBs involves the coalescence of a binary system of compact objects, *e.g.,* a black hole and a neutron star or two neutron stars [36, 37, 38, 39]. After the coalescence, the merged object is expected to collapse to a black hole surrounded by an accretion torus. An essential ingredient in this scenario is the formation of a central engine, which is required to launch a relativistic outflow with an energy of $\sim 10^{48}-10^{50}$ erg on a timescale of $\sim 0.1-1$ s [38, 39].

The qualitative scenario described above is generally supported by the association of SGRBs with old stellar populations, distinct from the young massive star associations for long GRBs [40, 41]. It is also supported to a good extent by fully general-relativistic simulations, which show that the formation of a torus of mass $M_{\rm tor} \lesssim 0.4 M_\odot$ around a black hole with spin $J/M^2 \simeq 0.7-0.8$, is inevitable [27].

In addition, recent simulations have also provided the first evidence that the merger of a binary of modestly magnetised neutron stars naturally forms many of the conditions needed to produce a jet of ultrastrong magnetic field, with properties that are broadly consistent with SGRB observations. This *missing link* between the astrophysical phenomenology of GRBs and the theoretical expectations is a genuine example of the new potential of numerical relativity and I will discuss it in detail below[1].

2.1 The numerical setup

It is not useful to discuss here in detail the numerical setup and the technical details of the numerical codes used in these calculations. These details can be found in Refs. [43, 26], while a description of the physical initial data was presented in Ref. [42]. It is sufficient to recall here that the evolution of the spacetime is obtained using a three-dimensional finite-differencing code providing the solution of a conformal traceless formulation of the Einstein equations [44] (*i.e.,* the `CCATIE` code). The equations of general-relativistic magnetohydrodynamics (GRMHD) in the ideal-MHD limit are instead solved using a code code [45, 46, 43] which adopts a flux-conservative formulation of the equations as presented in [47] and high-resolution shock-capturing schemes (*i.e.,* the `Whisky` code). In order to guarantee the divergence-free character of the MHD equations the flux-CD approach described in [48] was employed, although with the difference that the vector potential is used as evolution variable rather than the magnetic field. Both the Einstein and the GRMHD equations are solved using the vertex-centred adaptive mesh-refinement (AMR) approach provided by the `Carpet` driver [49]. In essence, the highest-resolution refinement level is centred around the peak in the rest-mass density of each star and in moving the "boxes" following the position of this maximum as the stars orbit. The boxes are evolved as a single refinement level when they overlap. The calculations were carried out using six levels of mesh refinement with the finest level having a resolution of $\Delta = 0.1500 M_{\odot} \simeq 221\,\mathrm{m}$.

From a physical point of view, the initial data is given by a configuration that could represent the properties of a neutron star-binary a few orbits before their coalescence. More specifically, we simulate two equal-mass neutron stars, each with a gravitational mass of $1.5 M_{\odot}$ (*i.e.,* sufficiently large to produce a black hole soon after the merger), an equatorial radius of $13.6\,\mathrm{km}$, and on a circular orbit with initial separation of $\simeq 45\,\mathrm{km}$ between the centres (all lengthscales are coordinate scales). Confined in each star is a poloidal magnetic field with a maximum strength of $10^{12}\,\mathrm{G}$. At this separation, the binary loses energy and angular momentum via emission of gravitational waves, thus rapidly proceeding on tighter orbits as it evolves.

[1] Much of what follows is taken from the discussion presented in Ref. [42].

2.2 The basic dynamics

After about 8 ms (~ 3 orbits) the two neutron stars merge forming a hypermassive neutron star (HMNS), namely, a rapidly and differentially-rotating neutron star, whose mass, $3.0\,M_\odot$, is above the maximum mass, $2.1\,M_\odot$, allowed with uniform rotation by an ideal-fluid equation of state (EOS)[2], $p = (\Gamma - 1)\rho\varepsilon$, where ρ is the baryonic density, ε the specific internal energy, and $\Gamma = 2$ with an adiabatic index of 2. Being metastable, a HMNS can exist as long as it is able to resist against collapse via a suitable redistribution of angular momentum [*e.g.,* deforming into a "bar" shape [22, 6]], or through the increased pressure-support coming from the large temperature-increase produced by the merger. However, because the HMNS is also losing angular momentum through gravitational waves, its lifetime is limited to a few ms, after which it collapses to a black hole with mass $M = 2.91\,M_\odot$ and spin $J/M^2 = 0.81$, surrounded by a hot and dense torus with mass $M_{\rm tor} = 0.063\,M_\odot$ [26].

These stages of the evolution can be seen in Fig. 1, which shows snapshots of the density colour-coded between 10^9 and $10^{10}\,{\rm gr/cm^3}$, and of the magnetic field lines (green on the equatorial plane and white outside the torus). Soon after the black hole formation the torus reaches a quasi-stationary regime, during which the density has maximum values of $\sim 10^{11}\,{\rm g/cm^3}$, while the accretion rate settles to $\dot{M} \sim 0.2\,M_\odot/{\rm s}$. Using the measured values of the torus mass and of the accretion rate, and assuming the latter will not change significantly, such a regime could last for $t_{\rm accr} \simeq M_{\rm tor}/\dot{M} \simeq 0.3$ s, after which the torus is fully accreted; furthermore, if the two neutron stars have unequal masses, tidal tails are produced which provide additional late-time accretion [27]. This accretion timescale is close to the typical observed SGRB durations [50, 38]. It is also long enough for the neutrinos produced in the torus to escape and annihilate in its neighbourhood; estimates of the associated energy deposition rate range from $\sim 10^{48}\,{\rm erg/s}$ [51] to $\sim 10^{50}\,{\rm erg/s}$ [52], thus leading to a total energy deposition between a few 10^{47} erg and a few 10^{49} erg over a fraction of a second. This energy would be sufficient to launch a relativistic fireball, but because radiative losses are accounted yet, the large reservoir of thermal energy in the torus cannot be extracted in these simulations.

The gravitational wave signal of the whole process is shown in the top part of the left panel in Fig. 2, while the bottom part exhibits the evolution of the MHD luminosity, $L_{\rm MHD}$, as computed from the integrated Poynting flux (solid line) and of the corresponding energy, $E_{\rm MHD}$, (dashed line). Clearly, the MHD emission starts only at the time of merger and increases exponentially after black-hole formation, when the gravitational wave signal essentially shuts off. Assuming that the quasi-stationary MHD luminosity is $\sim 4\times 10^{48}\,{\rm erg/s}$, the total MHD energy released during the lifetime of the torus is $\sim 1.2\times 10^{48}$ erg, which, if spread over an opening half-angle of $\sim 30^\circ$ (see discussion below), suggests a lower limit to the isotropic equivalent energy in the outflow of $\sim 9\times 10^{48}$ erg. While this is at the low end of the observed distribution of gamma-ray energies for SGRBs, larger MHD luminosi-

[2] The use of a simplified EOS does not influence particularly the results besides determining the precise time when the HMNS collapses to a black hole.

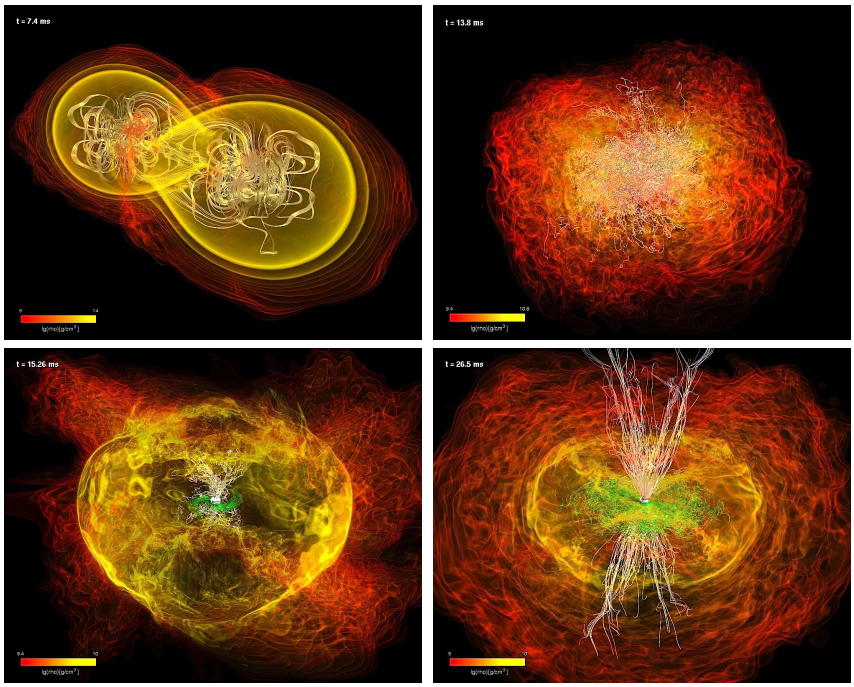

Fig. 1 Snapshots at representative times of the evolution of the binary and of the formation of a large-scale ordered magnetic field. Shown with a colour-code map is the density, over which the magnetic-field lines are superposed. The panels in the upper row refer to the binary during the merger ($t = 7.4$ ms) and *before* the collapse to black hole ($t = 13.8$ ms), while those in the lower row to the evolution *after* the formation of the black hole ($t = 15.26$ ms, $t = 26.5$ ms). Green lines sample the magnetic field in the torus and on the equatorial plane, while white lines show the magnetic field outside the torus and near the black hole spin axis. The inner/outer part of the torus has a size of $\sim 90/170$ km, while the horizon has a diameter of $\simeq 9$ km.

ties are expected either through the additional growth of the magnetic field via the winding of the field lines in the differentially-rotating disk (the simulation covers only one tenth of $t_{\rm accr}$), or when magnetic reconnection (which cannot take place within an ideal-MHD approach), is also accounted for [which may also increase the gamma-ray efficiency, *e.g.,* [53]].

The last two panels of Fig. 1 offer views of the accreting torus after the black-hole formation. Although the *matter* dynamics is quasi-stationary, the last two panels clearly show that the *magnetic-field* is not and instead evolves significantly. It is only when the system is followed well after the formation of a black hole, that MHD instabilities develop and generate the central, low-density, poloidal-field funnel. This regime, which was not accessible to previous simulations [54, 23, 24], is essential for the jet formation [55, 56]. Because the strongly magnetised matter in the torus is highly conductive, it shears the magnetic-field lines via differential rotation. A measurement of the angular-velocity in the torus indicates that it is essentially Keplerian and thus unstable to the magneto-rotational instability [57], which develops $\simeq 5$ ms after black-hole formation and amplifies exponentially both the poloidal and

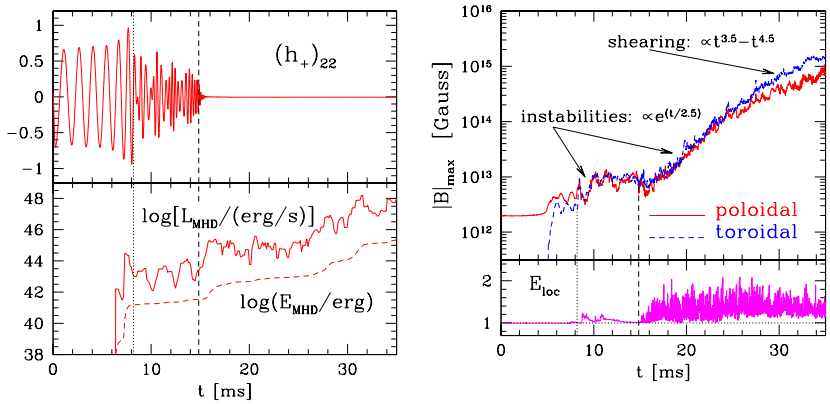

Fig. 2 *Left panel:* gravitational wave signal shown through the $\ell = 2, m = 2$ mode of the $+$ polarization, $(h_+)_{22}$, (top part) and of the MHD luminosity, $L_{\rm MHD}$, (bottom part) as computed from the integrated Poynting flux and shown with a solid line. The corresponding energy, $E_{\rm MHD}$, is shown with a dashed line. The dotted and dashed vertical lines show the times of merger (as deduced from the first peak in the evolution of the gravitational wave amplitude) and black-hole formation, respectively. *Right panel:* Evolution of the maximum of the magnetic field in its poloidal (red solid line) and toroidal (blue dashed line) components. The bottom panel shows the maximum local fluid energy indicating that an unbound outflow (*i.e.,* $E_{\rm loc} > 1$) develops and is sustained after black-hole formation.

the toroidal magnetic fields; the e-folding time of the instability is $\simeq 2.5$ ms and in good agreement with the one expected in the outer parts of the torus [57]. Because of this exponential growth, the final value of the magnetic field is largely insensitive to the initial strength and thus a robust feature of the dynamics (see also [58] for a similar behaviour recently computed in a HMNS)

A quantitative view of the magnetic-field growth is shown in the right panel of Fig. 2, which shows the evolution of the maximum values in the poloidal and toroidal components. Note that the latter is negligibly small before the merger, reaches equipartition with the poloidal field as a result of a Kelvin-Helmholtz instability triggered by the shearing of the stellar surfaces at merger [54, 59], and finally grows to $\simeq 10^{15}$ G by the end of the simulation. At later times ($t \gtrsim 22$ ms), when the instability is suppressed, the further growth of the field is due to the shearing of the field lines and it increases only as a power-law with exponent 3.5 (4.5) for the poloidal (toroidal) component. Although the magnetic-field growth essentially stalls after $t \simeq 35$ ms, further slower growths are possible [60], yielding correspondingly larger Poynting fluxes. Indeed, when the ratio between the magnetic flux across the horizon and the mass accretion rate becomes sufficiently large, a Blandford-Znajek mechanism [61] may be ignited [62]; such conditions are not met over the timescale of the simulations, but could develop over longer timescales. Also shown in the right panel of Fig. 2 is the maximum local fluid energy, highlighting that an *unbound outflow* (*i.e.,* $E_{\rm loc} > 1$) develops after black-hole formation along the outer walls of the torus and persists for the whole duration of the simulation.

Finally, Fig. 3 provides a summary of the magnetic-field dynamics. It shows the magnetic field in the HMNS formed after the merger and its structure and dynamics

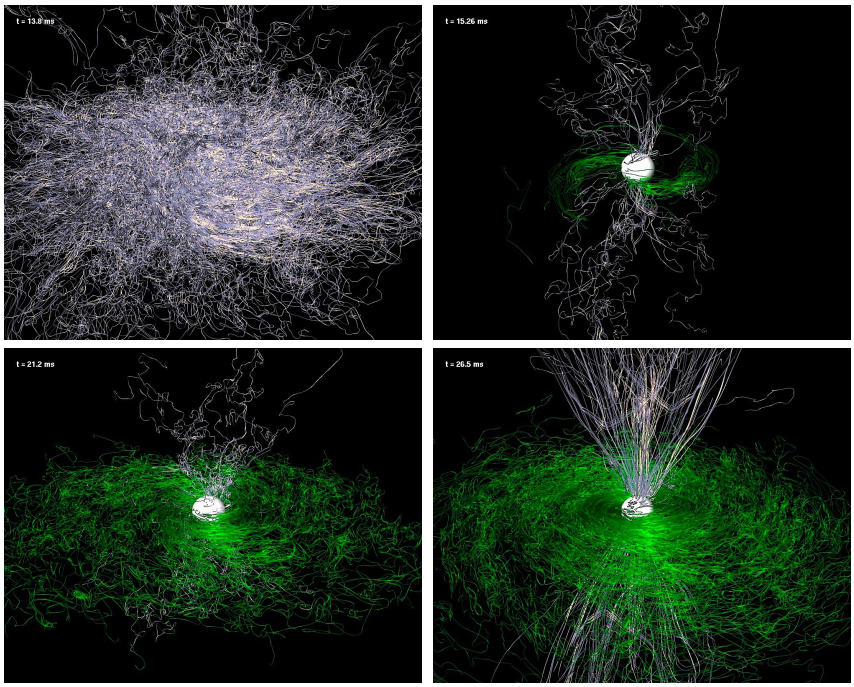

Fig. 3 Magnetic-field structure in the HMNS (first panel) and after the collapse to black hole (last three panels). Green refers to magnetic-field lines inside the torus and on the equatorial plane, while white refers to magnetic-field lines outside the torus and near the axis. The highly turbulent, predominantly poloidal magnetic-field structure in the HMNS ($t = 13.8$ ms) changes systematically as the black hole is produced ($t = 15.26$ ms), leading to the formation of a predominantly toroidal magnetic field in the torus ($t = 21.2$ ms). All panels have the same linear scale, with the horizon's diameter being of $\simeq 9$ km.

after the collapse to black hole. In particular, in the last three panels it shows the magnetic-field structure inside the torus and on the equatorial plane (green), and outside the torus and near the axis (white). It is apparent that the highly turbulent magnetic field in the HMNS ($t = 13.8$ ms) changes systematically as the black hole is produced ($t = 15.26$ ms), leading to the formation of a toroidal magnetic field in the torus ($t = 21.2$ ms)[3]. As the MRI sets in, the magnetic field is not only amplified, but also organises itself into a dual structure, which is mostly toroidal in the accretion torus with $B_{\rm tor} \sim 2 \times 10^{15}$ G, but predominantly poloidal and jet-like along the black-hole spin axis, with $B_{\rm pol} \sim 8 \times 10^{14}$ G ($t = 26.5$ ms)[4]. Note that the generation of an ordered large-scale field is far from trivial and a nonlinear dynamo may explain why the MRI brings a magnetic field self-organization, as it has been also suggested in case of MRI-mediated growth of the magnetic field in the conditions

[3] Turbulence in relativistic flows is an extremely challenging problem that is also essentially unexplored. Also in this case, the first relativistic simulations have been performed only recently [63, 64].

[4] A similar magnetic-field configuration has been recently reproduced also when simulating the merger of a magnetised neutron star onto a black hole [65].

met in the collapse of massive stellar cores [66, 60]. However, the jet-like structure produced in the simulation is not yet the highly collimated ultrarelativistic outflow expected in SGRBs (see also below).

The magnetic hollow jet-like structure has an opening half-angle of $\sim 30^\circ$, which sets an upper limit for the opening half-angle of any potential outflow, either produced by neutrino energy deposition [55] or by electromagnetic processes [56]. In these simulations most of the outflow develops along the edges of the jet-like structure, via a turbulent layer of electromagnetic driven matter, which shields the central funnel from excessive baryonic pollution. It is reasonable to expect that such a layer is crucial to set the opening angle of any ultrarelativistic jet, to shape both the radial and transverse structure of the jet, as well as to determine its stability properties. The Lorentz factors of the outflow measured in these simulations are not very high ($\gamma \lesssim 4$), but can potentially be amplified by several orders of magnitude in the inner baryon-poor regions through special-relativistic effects [67], the variability of the flow [68], or when resistive-MHD effects are taken into account [69]. Such accelerations will be produced as a more realistic and general-relativistic treatment of the radiative losses will become computationally affordable.

2.3 Comparison with observations

Below I briefly discuss how the results presented above broadly match the properties of the central engine as deduced from the observations.

Duration: The observed duration of the prompt gamma-ray emission GRBs is energy dependent and is usually determined through T_x, the time over which x% of the total counts are observed, between the $(100-x)/2$ and $(100+x)/2$ percentiles. The most common intervals used are T_{90} (or T_{50}), initially defined [50] between 20 keV and 2 MeV. The GRB duration distribution is bimodal [50], where the durations of SGRBs (approximately 25% of GRBs) are well-fit by a fairly wide log-normal distribution centred around $T_{90} \approx 0.8$ s with a FWHM of 1.4 dex [38]. The typical redshifts of the SGRBs observed with *Swift* are in the range $z \sim 0.3-1$, suggesting a central value of the intrinsic duration distribution of $\approx \langle 1+z\rangle^{-1} 0.8$ s ~ 0.5 s, and a comparably wide distribution around this value. This is in close agreement with our accretion time of ~ 0.3 s.

Energy: The isotropic equivalent energy output in the prompt gamma-ray emission of SGRBs, $E_{\gamma,\rm iso}$, spans a wide range, from $(2.7\pm 1)\times 10^{48}$ erg (in the observed energy range $15-350$ keV) for GRB 050509B at a redshift of $z=0.225$ [70], up to $(1.08\pm 0.06)\times 10^{53}$ erg (in the observed energy range 10 keV – 30 GeV) for GRB 090510 at $z=0.903$ [71]. However, the most typical values are in the range $E_{\gamma,\rm iso} \sim 10^{49}-10^{51}$ erg [38]. In this model, the highly relativistic outflow may be powered either by neutrino-anti neutrino annihilation, or by the Blandford-Znajek mechanism. For the former one might expect a total energy release between a few 10^{47} erg and $\sim 10^{49}$ erg [72, 73], into a bipolar relativistic jet of opening half-angle $\theta_{\rm jet} \sim 8-30^\circ$, corresponding to a fraction $f_b \sim 0.01-0.13$ of the total solid angle,

and isotropic equivalent energies, $E_{\nu\bar{\nu},\mathrm{iso}}$, between a few 10^{48} erg and $\sim 10^{51}$ erg. For the latter mechanism, instead, and if the magnetisation near the event horizon becomes sufficiently high, the jet power for these values for the black-hole mass and spin is [74]

$$L_{\mathrm{BZ}} \sim 3.0 \times 10^{50} \left(\frac{f_{\mathrm{rel}}}{0.1}\right) \left(\frac{B}{2 \times 10^{15}\,\mathrm{G}}\right)^2 \mathrm{erg/s}\,, \tag{1}$$

where f_{rel} is the fraction of the total Blandford-Znajek power that is channelled into the resulting relativistic jet (and $f_{\mathrm{rel}} \sim 0.1$ might be expected for ejecta with asymptotic Lorentz factors above 100). This relativistic outflow is launched over a timescale of $\sim 0.2\,\mathrm{s}$ and corresponds to

$$E_{\mathrm{BZ,iso}} \sim 1.2 \times 10^{51} \left(\frac{f_{\mathrm{rel}}}{0.1}\right) \left(\frac{f_b}{0.05}\right)^{-1} \left(\frac{B}{2 \times 10^{15}\,\mathrm{G}}\right)^2 \mathrm{erg}\,, \tag{2}$$

Comparing the X-ray afterglow luminosity (after 10 or 11 hours) and $E_{\gamma,\mathrm{iso}}$ suggests that the efficiency of the prompt gamma-ray emission in SGRBs is typically high [70], and similar to that of long GRBs [75], with $E_{\gamma,\mathrm{iso}} \sim (0.1-0.9)E_{\mathrm{iso}}$, radiating between $\sim 10\%$ and $\sim 90\%$ of the initial energy of the ultrarelativistic outflow. Therefore, this model is able to accommodate the observed $E_{\gamma,\mathrm{iso}}$ values.

Lorentz factor: The Fermi Gamma-Ray Space Telescope has detected GeV emission from SGRBs [76], suggesting typical lower limits of $\gamma_{\mathrm{min}} \sim 10^2 - 10^3$. In particular, $\gamma_{\mathrm{min}} \approx 1200$ was obtained for GRB 090510 [71]. However, a more realistic model [77] results in γ_{min} values lower by a factor of ~ 3. Therefore, the central engine should be capable of producing outflow Lorentz factors of at least a few hundred. The fact that our simulation produces a strongly magnetised mildly relativistic outflow at angles near $\sim 30^\circ$ from the black-hole spin axis would help shield the inner region near the spin axis from excessive baryon loading, and thus assist in achieving high asymptotic Lorentz factors at large distance from the source, after the outflow in this region is triggered by neutrinos and/or the Blandford-Znajek mechanism.

Jet angular structure: This is poorly constrained by observations (even more so than for long GRBs). The only compelling case for a jet break in the afterglow light-curve is for GRB 090510 [78], which occurred very early on (after $\sim 1400\,\mathrm{s}$), and would thus imply an extremely narrow jet ($\theta_{\mathrm{jet}} \sim 0.2-0.4^\circ$) and modest true energy output in gamma-rays ($\sim 10^{48}$ erg). If this is indeed a jet break, it might correspond to a line of sight near a very narrow and bright core of a jet, which also has significantly wider wings. Observers with lines of sight along these wings would then see a much dimmer and more typical SGRB [79, 80]; without such wings, however, the observations would suggest a very large intrinsic and beaming-corrected event rate per unit volume. In most cases there are only lower limits on a possible jet break time [38], resulting in typical limits of $f_b \gtrsim 10^{-2}$ or $\theta_{\mathrm{jet}} \gtrsim 8^\circ$. This is consistent with the expectation of $\theta_{\mathrm{jet}} \sim 8-30^\circ$ for the ultrarelativistic ejecta capable of producing a SGRB (which would also imply a reasonable SGRBs intrinsic event rate per unit volume).

2.4 Summary

The calculations reported above demonstrate that a binary merger of two neutron stars inevitably leads to the formation of a relativistic jet-like and ultrastrong magnetic field, which could serve as a central engine for SGRBs. Because the magnetic-field growth is exponential, the picture emerging from these simulations is rather general and applies equally even to mildly magnetised neutron stars. Overall, this first "little piece" of numerical relativity removes a significant uncertainty as to whether such binary mergers can indeed produce the central engines of SGRBs. While the electromagnetic energy release is already broadly compatible with the observations, the simulations discussed above lack a proper treatment of the energy losses via photons and neutrinos or resistive dissipation, which can provide a fundamental contribution to the energy-input necessary to launch the fireball and cool the torus [52, 51]. This additional energy input, whose self-consistent inclusion in general relativity remains extremely challenging, may help to launch an ultrarelativistic outflow very early after the black hole forms and complete the picture of the central engine of a SGRB.

3 Second piece: A dynamical hoop conjecture

The second "little piece" of numerical relativity that I will discuss aims at addressing the issue of necessary conditions for the formation of a black hole, which still represents one of the most intriguing and fascinating predictions of classical general relativity. There is abundant astronomical evidence that black holes exist, and a number of considerations supporting the idea that under suitable conditions gravitational collapse is inevitable [81]. In addition, there is overwhelming numerical evidence that black-hole formation does take place in a variety of environments [42]. Yet, a rigorous definition of the sufficient conditions for black-hole formation is still lacking. Hence, it is not possible to predict whether the collision of two compact objects, either stars or elementary particles, will lead to the formation of a black hole.

The *hoop conjecture* proposed by Thorne in the '70s, provides some reasonable and intuitive guidelines [82]. I recall that the conjecture states that a black hole is formed if an amount of "mass-energy" E can be compressed to fit within a hoop with radius equal or smaller than the corresponding Schwarzschild radius, *i.e.,* if $R_{\rm hoop} \leq R_{\rm s} = 2GE/c^4$, where G is gravitational constant and c the speed of light. Even though it can be made precise under particular circumstances [83], the hoop conjecture is not meant to be a precise mathematical statement and, in fact, it is difficult to predict if the above-mentioned collision will compress matter sufficiently to fit within the limiting hoop. Loosely speaking, what is difficult is to determine which part of the "kinetic energy" of the system can be accounted to fit within the hoop. Since at the collision the conversion of kinetic energy into internal energy is

a highly nonlinear process, any quantitative prediction becomes rapidly inaccurate as the speeds involved approach that of light.

As stated above, the hoop conjecture is purely classical. A quantum-mechanical equivalent is not difficult to formulate, although not very stringent, as it simply implies that a black hole will be formed at Planck-energy scales. The predicting power does not improve significantly when considering the conditions of black-hole formation in higher-dimensional theories of gravity (see, *e.g.,* [84, 85, 86]). In these frameworks, the energy required for black-hole formation might be significantly smaller [84], thus providing the possibility of producing them in the Large Hadron Collider (LHC) [87], but no firm conclusion has been reached yet.

Clearly, although numerical simulations represent a realistic route to shed some light on this issue (see, *e.g.,* , [88, 89, 90]), even the simplest scenario of the collision of two compact objects at ultrarelativistic speeds is far from being simple and it is actually very challenging. A first step was taken by Eardley and Giddings [91], who have studied the formation of a black hole from the head-on collision of two plane-fronted gravitational waves with nonzero impact parameter (previous work of D'Eath and Payne [92, 93, 94] using different methods had considered a zero impact parameter). In all of these analyses each incoming particle is modelled as a point particle accompanied by a plane-fronted gravitational shock wave corresponding to the Lorentz-contracted longitudinal gravitational field of the particle. At the instant of collision the two shock waves pass through one another and interact through a nonlinear focusing and shearing. As a result of their investigation, a lower bound was set on the cross-section for black-hole production, *i.e.,* $\sigma > 32.5(GE/2c^4)^2$, where E is the centre-of-mass (lab) energy. More recently, and in a framework which is closer to the one considered here, this problem has been investigated by Choptuik and Pretorius [95], who studied the collision of two classical spherical solitons, with a total energy of the system in the lab frame $E = 2\gamma_b m_0 c^2$, where m_0 is the "rest-mass", $\gamma_b \equiv 1/\sqrt{1-v_b^2/c^2}$ and v_b the boost velocity. They were then able to show that for collisions with sufficiently high boost, *i.e.,* $\gamma_b \gtrsim 2.9$, a black hole can be formed.

In what follows I discuss what has been recently reported on the first calculations of black-hole production from the collision of two compact, selfgravitating, fluid objects boosted at ultrarelativistic speeds[5] (A similar investigation by East and Pretorius [97] has also appeared at about the same time).

I start by pointing out that there are several important differences with the previous investigations in [92, 93, 94, 91, 95]. Differently from [92, 93, 94, 91], in fact, I will consider colliding objects that are not in vacuum and are not treated as point particles. Rather, they are relativistic stars, which obviously extended and selfgravitating objects, thus with a behaviour that is intrinsically different. Also, differently from [95], these objects are not described as scalar fields, but as fluids and thus represent a more realistic description of baryonic matter, such as the one employed when simulating relativistic heavy-ion collisions [98]. These intrinsic differences also make the comparison with the works of [92, 93, 94, 91] very hard if possible

[5] Much of what follows is taken from the discussion presented in Ref. [96].

at all. On the other hand, many analogies exist with the collision of bosons stars considered in [95], and that, as I will discuss below, can be interpreted within the more general description of black-hole production from ultrarelativistic collisions.

Overall, the most important and distinguishing feature in the collision of two self-gravitating stars is that a black hole can be produced even from zero initial velocities if the initial masses are large enough; this behaviour is clearly absent in all previous results, where instead a critical initial boost is necessary [92, 93, 94, 91, 95]. In addition, for each value of the effective Lorentz factor, $\langle\gamma\rangle$, a critical initial mass exists, $M_{\rm c}$, above which a black hole is formed and below which matter, at least in part, selfgravitates. More importantly, both $M_{\rm c}$ follows a simple scaling with $\langle\gamma\rangle$, thus allowing to extrapolate the results to the masses and energies of modern particle accelerators and to deduce that black-hole production is unlikely at LHC scales.

3.1 The numerical setup

The numerical setup employed in the simulations is the same presented in [99], and it uses an axisymmetric code to solve in two spatial dimensions, (x,z), the set of the Einstein and of the relativistic-hydrodynamic equations [100]. The axisymmetry of the spacetime is imposed exploiting the "cartoon" technique, while the hydrodynamics equations are written explicitly in cylindrical coordinates. All the simulations use an ideal-fluid EOS with $\Gamma = 2$. The initial configurations consist of spherical stars, constructed as in [99, 101] after specifying the central density, ρ_c, where the latter also serves as parameter to determine the critical model. The stars have an initial separation D and are boosted along the z-direction via a Lorentz transformation with boost $v_{\rm b}/c$. To limit the initial violation in the constraints, D is chosen to be sufficiently large, *i.e.,* $D = 240\,M_\odot$, and an optimal superposition of the two isolated-star solutions that will be presented in a longer paper. The grid has uniform spacing $\Delta = 0.08(0.06)\,M_\odot$ with extents $x/M_\odot \in [0,80]$ and $z/M_\odot \in [0,150(200)]$, where the round brackets refer to the more demanding high-boost cases. Reflection boundary conditions are applied on the $z = 0$ plane, while outgoing conditions are used elsewhere.

3.2 The basic dynamics

The dynamics of the process is rather simple. As the two stars approach each other, the initial boost velocity increases as a result of the gravitational attraction, leading to a strong shock as the surfaces of the stars collide. In the case of *supercritical* initial data, *i.e.,* of stars with masses above a critical value, $M_{\rm c}$, a black hole is promptly produced and most of the matter is accreted. Conversely, in the case of *subcritical* initial data, *i.e.,* of stars with masses below $M_{\rm c}$, the product of the collision is a hot and extended object with large-amplitude oscillations. Part of the stellar matter

is unbound and leaves the numerical grid as the product of the collision reaches an equilibrium.

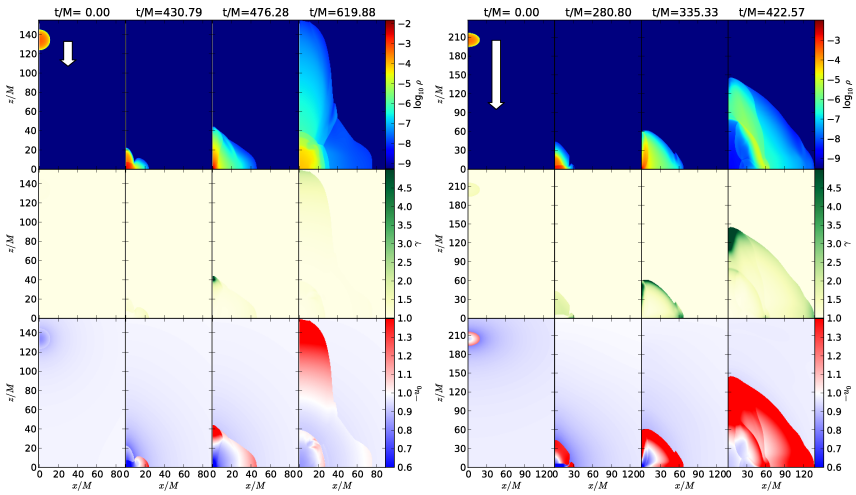

Fig. 4 Representative snapshots of the rest-mass density, ρ in units where $c = 1 = M_\odot$ (top row), of the Lorentz factor, γ (middle row), and of the local fluid energy, $-u_0$ (bottom row), for subcritical models with an initial small boost $v_{\rm b}/c = 0.3$ (left panel) or a large one $v_{\rm b}/c = 0.8$ (right panel). Note that the post-collision flow is essentially jet-like for the low-boost case (left panel), while essentially spherical for the high-boost case (right panel); in this latter case, most of the matter is unbound.

Figure 4 shows snapshots at representative times of the rest-mass density, ρ (top row), of the Lorentz factor, $\gamma \equiv (1 - v^i v_i/c^2)^{-1/2}$ (middle row), and of the local fluid energy, $-u_0$ (bottom row), for two subcritical models. The left panel, in particular, refers to a binary boosted at $v_{\rm b}/c = 0.3$. Note that the stars are strongly compressed by the collision, with the rest-mass density increasing exponentially. The merged object expands in a jet-like fashion along the z-direction, with the bulk of the matter being accelerated up to $\gamma \sim 16$, or equivalently, $v/c \sim 0.998$, but then settling on much slower flows with $\gamma \lesssim 2.1$. Furthermore, the front of the jet has $-u_0 > 1$ indicating that part of the shocked matter has sufficient energy to have become gravitationally unbound. As a result, the rest-mass density at the center of the merged object is smaller than the maximum density of the initial configuration, although the origin still represents the region where the density is the largest. The right panel, on the other hand, refers to a highly-boosted binary, *i.e.,* with $v_{\rm b}/c = 0.8$, with each star being initially highly distorted by the Lorentz contraction. Also in this case, the stars are strongly compressed by the collision, but the merged object expands in a spherical blast-wave fashion, with an almost spherical distribution of matter and bulk Lorentz factor. The latter reaches values as large as $\gamma \sim 30$, or equivalently, $v/c \sim 0.999$, which, in contrast with the low-boost case, do not decrease in time. As a comparison, the typical bulk Lorentz factors obtained in the merger of binary neutron stars in quasi circular orbits is $\gamma \sim 1.03$ [27]. The very large kinetic energies

involved in the collision are sufficient to make a very large portion of the stellar matter unbound, as clearly shown by the bottom-right panel of Fig. 4, which reports the local fluid energy. The rest-mass density distribution in the expanding blast wave has a minimum at the origin, where a large rarefaction is produced by the matter expanding as an ultrarelativistic thick shell.

The marked transition from a jet-like outflow, not too dissimilar from the simple Bjorken flow used to model the very early states of relativistic ion-collisions [102], to a shell-like structure, not too dissimilar from "transverse expansion" modelled in the subsequent stages of relativistic ion-collisions (see [103] and references therein), signals that it is not unreasonable to extrapolate some of the results presented here also to the collision of ultrarelativistic elementary particles.

The transition from the two qualitatively-different regimes discussed above is further confirmed by the evolution of the rest-mass normalized to the initial value M_0. The simulations in fact reveal that the unbound fraction is just a few percent of the total rest-mass in the case of a low-boost collision, with most of the matter being confined in the selfgravitating "star". This is to be contrasted with what happens for a high-boost collision, where the unbound fraction is $\sim 100\%$ of the total rest-mass. This behaviour provides a strong indication that, at least for subcritical collisions, the role played by gravitational forces is a minor one as the kinetic energy is increased. This is what happens in the collision of two particles at ultrarelativistic speeds, where all of the matter is obviously unbound.

3.3 Critical behaviour and scaling

A remarkable property of the head-on collision of compact stars is the existence of type-I critical behaviour, which was first pointed out in [104] and subsequently extended in [100]. In essence, in these works it was found that when considering stars with initial zero velocity at infinity, it is possible to fine-tune the initial central density $\rho_{\rm c}$ (and hence the mass) near a critical value, $\rho_{\rm c}^\star$, so that stars with $\rho_c > \rho_c^\star$ would collapse *eventually* to a black hole, while the models with $\rho_c < \rho_c^\star$ would *eventually* lead to a stable stellar configuration. As a result, the head-on collision of two neutron stars near the critical threshold can be seen as a transition in the space of configurations from an initial stable solution over to a critical metastable one which can either migrate to a stable solution or collapse to a black hole [101]. As the critical limit is approached, the survival time of the metastable object, $\tau_{\rm eq}$, increases as $\tau_{\rm eq} = -\lambda \ln|\rho_c - \rho_c^\star|$, with $\lambda \sim 10$ [104, 100].

Although the free-fall velocities considered in [104, 100] were very small, the critical behaviour continues to hold also when the stars are boosted to ultrarelativistic velocities. Interestingly, the threshold $\rho_{\rm c}^\star$ becomes now a function of the initial effective boost. Determining $\rho_{\rm c}^\star$ becomes especially challenging as the Lorentz factor is increased and the dynamics of the matter becomes extremely violent, with very strong shocks and rarefaction waves. However, it was possible to determine the threshold for all the range of initial boosts considered, *i.e.,* $v_{\rm b}/c \in [0, 0.95]$,

$\gamma_b \in [1, 3.2]$, and even to a reasonable accuracy, *e.g.,* $\rho_c^\star = (3.288023 \pm 0.000003) \times 10^{14}\,\mathrm{g/cm^3}$, for the initial boost of $v_\mathrm{b}/c = 0.3$.

The existence of critical behaviour near which the details of the initial conditions become irrelevant and which is the *same* at different boosts, *i.e.,* λ does not depend on γ nor on ρ_c (Refs. [104, 105] have shown there is "universality" when varying γ and fixing ρ_c), gives us a wonderful tool to explore the conditions of black-hole formation also far away from the masses and Lorentz factors considered in this paper. This is illustrated in Fig. 5, which reports the gravitational mass of the isolated spherical star as a function of the effective initial Lorentz factor

$$\langle\gamma\rangle \equiv \frac{\int dV\, T_{\mu\nu} n^\mu n^\nu}{(\int dV\, T_{\mu\nu} n^\mu n^\nu)_0}\,, \tag{3}$$

where $T_{\mu\nu}$ is the stress-energy tensor, n^μ is the unit normal to the spatial hyperspace with proper volume element dV, and the index 0 refers to quantities measured in the initial unboosted frame. I should stress that the definition of the effective Lorentz factor (3) is necessary because the stars are extended and thus the Lorentz factor will be different in different parts of the star. Expression (3), on the other hand, can be taken as ratio of the energies measured in the boosted and unboosted frames, and hence a generalisation of the Lorentz factor for a point particle (Indeed $\langle\gamma\rangle \to 1$ for $v_b \to 1$). Of course, other parametrizations are possible, still leading to scaling laws, but with slightly different exponents. Filled circles indicate initial data leading to a black hole, while triangles indicate initial data leading to a "star", whereby I mean an object which is at least in part selfgravitating (orange errorbars provide an approximate upper limit of $\sim 8\%$ to the error in the measurements). Also indicated as a blue solid line is the critical line separating the two regions of black hole and star formation (the latter is shown as a shaded region). Clearly, the numerical results provide a tight fit of the critical line with a power law

$$\frac{M_\mathrm{c}}{M_\odot} = K\,\frac{1}{\langle\gamma\rangle^n} \approx 0.92\,\frac{1}{\langle\gamma\rangle^{1.03}}\,. \tag{4}$$

Expression (4) offers itself to a number of considerations. First, it essentially expresses the conservation of energy. Second, in the limit of zero initial velocities, $\langle\gamma\rangle \to 1$, one obtains that $M_\mathrm{c} \simeq 0.92\,M_\odot$, so that the corresponding total mass, $2M_\mathrm{c}$, is only $\sim 12\%$ larger than the maximum mass of the relative spherical-star sequence, *i.e.,* $M_\mathrm{max} = 1.637\,M_\odot$. Third, in the opposite limit of $\langle\gamma\rangle \to \infty$, expression (4) predicts that the critical mass will go zero. This is indeed what one would expect: as the kinetic energy diverges, no room is left for selfgravitating matter, which will all be ejected but for an infinitesimal amount which will go into building the zero-mass critical black hole. Fourthly, (4) is also in agreement with the results in [95, 97], whereby one can recognize the black-hole formation as the crossing of the critical line when moving to larger Lorentz factors while keeping the rest-mass constant.

Finally, using (4) it is possible to probe whether the kinetic energies achieved by modern particle accelerators, such as the LHC, are sufficient to produce micro black holes from the collision of two ultrarelativistic particles. Using the results reported

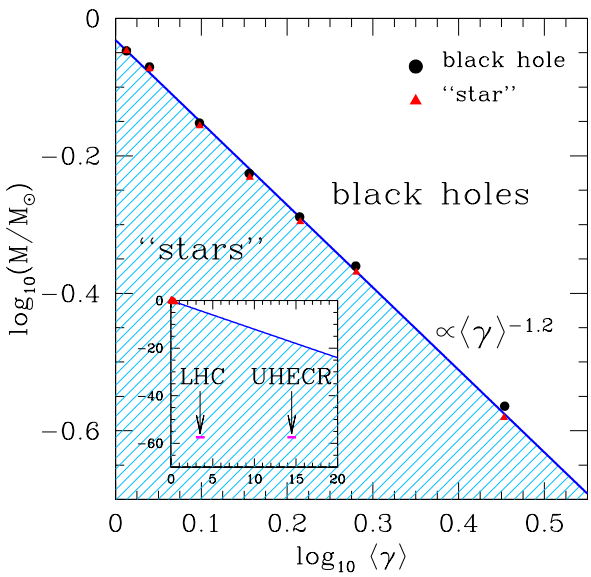

Fig. 5 Critical line as a function of the average Lorentz factor, with circles indicating black holes and triangles self-gravitating objects. The inset shows the regimes explored at LHC and measured in UHECR.

in Ref. [106], the expected energies achieved by LHC in the next couple of years will be $4-7\,\mathrm{TeV}$, so that a proton, whose mass is ~ 938 MeV $\sim 8.41\times 10^{-58}\,M_\odot$, can be accelerated up to $\gamma\sim 7.5\times 10^3$. I have therefore reported the range of masses and Lorentz factors accessible to LHC in the inset in Fig. 5, where it appears as a small magenta box. Note that the calculations reported here do not intend to be a realistic approximation of the dynamics of ultrarelativistic particle collisions. However, these calculations and the presence of a critical behaviour can be used to deduce that the ranges reachable at the LHC are well below the critical line and thus in the region where a partially-confined collided object is expected.

Of course, this line of arguments wildly extrapolates our results by almost 60 orders of magnitude in mass (11 in Lorentz factor) and neglects quantum effects and extra-dimension effects that might be important at Planck-energy scales. Bearing in mind these caveats, our calculations suggest that the production of micro black holes at LHC will be unlikely. An additional confirmation that our estimates are not unreasonable comes from considering the corresponding energy and Lorentz factors for the observed ultra-high energy cosmic rays (UHECR), that are observed with energies up to $\sim 10^{20}\,\mathrm{eV}$ (*i.e.,* $\gamma\sim 10^{11}$) and for which there is no evidence of black-hole formation when interacting with the atmosphere [107]. Also in this case, the relevant range of masses and Lorentz factors is shown in the inset and falls in the region where no black holes should be produced.

As a final remark I note that the scaling relation (4) can be expressed equivalently in terms of the original stellar compactness, M/R as

$$\left(\frac{M}{R}\right)_{\rm c} = K' \, \frac{1}{\langle\gamma\rangle^{n'}} \approx 0.08 \, \frac{1}{\langle\gamma\rangle^{1.13}} \, . \tag{5}$$

Since $M_{\rm lab} \equiv \langle\gamma\rangle M$ is the mass in the lab frame, and since R is the largest dimension in that frame being the transverse one to the motion, the ratio

$$\left(\frac{M_{\rm lab}}{R}\right)_{\rm c} = K' \frac{1}{\langle\gamma\rangle^{n'-1}} \sim K' \frac{1}{\langle\gamma\rangle^{0.13}} \, , \tag{6}$$

provides the condition for the amount of energy that, when confined in a hoop of radius R, would lead to a black hole. Hence, expression (6) extends the spirit of the hoop conjecture to the case in which a kinetic energy is present. Note that the limiting value $\langle\gamma\rangle = 1$ does not corresponds to a static configuration (as in the hoop conjecture) but to a binary that is at rest at infinity. This explains why in this limit $(M_{\rm lab}/R)_{\rm c} = (M/R)_{\rm c} \simeq 0.08$, which is considerably smaller than the value $1/2$ predicted by the hoop conjecture.

3.4 Summary

The calculations reported above demonstrate that it is possible to find a criterion for the conditions leading to black-hole formation in the collision of two selfgravitating fluids moving at ultrarelativistic velocities. The Lorentz factors reached in these simulations are considerably larger than those encountered in merging neutron-star binaries, especially if the inspiral is along quasi-circular orbits. The properties of the flow after the collision change with Lorentz factor, with most of the matter being ejected in a spherical blast wave for large boosts. Interestingly, the collided object exhibits a critical behaviour of type I, which is found to persist also as the initial boost is increased. This allows one to derive a simple scaling law and extrapolate these results to the energies of elementary particles at LHC and conclude that black-hole production is unlikely in that case.

4 Third piece: horizons as probes of black-hole dynamics

The third and last "little piece" of numerical relativity that I will discuss is instead about calculations in vacuum spacetimes and focuses on the merger of two black holes. This process, which represents one of the most important source of gravitational waves, is generally accompanied by the recoil of the final black hole as a result of anisotropic gravitational wave emission. While this scenario has been investigated for decades [108] and first estimates have been made using approximated and

semi-analytical methods such as a particle approximation [109], post-Newtonian methods [110] and the close-limit approximation (CLA) [111], it is only thanks to the recent progress in numerical relativity that accurate values for the recoil velocity have been computed [112, 113, 114, 115, 116, 117, 118, 119, 120].

Besides being a genuine nonlinear effect of general relativity, the generation of a large recoil velocity during the merger of two black holes has a direct impact in astrophysics. Depending on its size and its variation with the mass ratio and spin, in fact, it can play an important role in the growth of supermassive black holes via mergers of galaxies and on the number of galaxies containing black holes. Numerical-relativity simulations of black holes inspiralling on quasi-circular orbits have already revealed many of the most important features of this process showing, for instance, that asymmetries in the mass can lead to recoil velocities $v_{\rm k} \lesssim 175\,{\rm km/s}$ [112, 113], while asymmetries in the spins can lead respectively to $v_{\rm k} \lesssim 450\,{\rm km/s}$ or $v_{\rm k} \lesssim 4000\,{\rm km/s}$ if the spins are aligned [115, 116, 118] or perpendicular to the orbital angular momentum [121, 122, 114] (see [123] for a review and [124] for the most recent results).

At the same time, however, there are a number of aspects of the nonlinear processes leading to the recoil that are far from being clarified even though interesting work has been recently carried out to investigate such aspects [125, 126, 127]. One of these features, and possibly the most puzzling one, is the generic presence of an *"anti-kick"*, namely, of one (or more) decelerations experienced by the recoiling black hole. Such anti-kicks take place after a single apparent horizon has been found and have been reported in essentially all of the mergers simulated so far (see Fig. 8 of Ref. [118] for some examples).

What follows discusses a phenomenological framework which provides a novel description of the stages during which the anti-kick is generated, and that can be used to formulate a simple and qualitative interpretation of the physics underlying this process. I will focus on the head-on collision of two nonspinning black holes with different mass. Although this is the simplest scenario for a black-hole merger, it contains all the important aspects that can be encountered in more generic conditions[6].

4.1 The basic picture

I will start by presenting a qualitative interpretation of the antikick by considering the simple head-on collision of two Schwarzschild black holes with unequal masses. This qualitative picture will be made quantitative and gauge-invariant by studying the logical equivalent of this process in the evolution of a Robinson-Trautman spacetime, with measurements of the recoil made at future null infinity. The insight gained with this spacetime will be valuable to explain the anti-kick under generic conditions and to contribute to the understanding of nonlinear black-hole physics.

[6] Much of what follows is taken from the discussion presented in Refs. [128, 129, 130].

Figure 6 illustrates the dynamics of the head-on collision using a schematic cartoon where I am considering a coordinate system centred in the total centre of mass of the system and where the smaller black hole is initially on the positive z-axis, while the larger one is on the negative axis. As the two black holes free-fall towards each other, the smaller one will move faster and will be more efficient in "forward-beaming" its gravitational wave emission [110]. As a result, the linear momentum will be radiated mostly downwards, thus leading to an upwards recoil of the black hole binary [*cf.,* stage (1) in Fig. 6]. At the merger, the black-hole velocities will be the largest and so will also be the anisotropic gravitational wave emission and the corresponding recoil of the system. However, when a single apparent horizon is formed comprising the two black holes, the curvature distribution on this 2-surface will be highly *anisotropic*, being higher in the upper hemisphere (*cf.,* red-blue shading in stage (2) of Fig. 6). Because the newly formed black hole will want to radiate all of its deviations away from the final Schwarzschild configuration, it will do so more effectively there where the curvature is larger, thus with a stronger emission of gravitational waves from the northern hemisphere. As a result, after the merger the linear momentum will be emitted mostly upwards and this sudden change in sign will lead to the anti-kick. The anisotropic gravitational wave emission will decay exponentially as the curvature gradients are erased and the quiescent black hole reaches its final and decelerated recoil velocity [*cf.,* stage (3)][7].

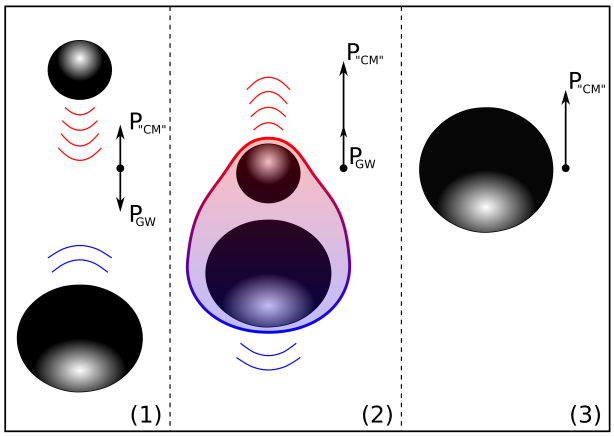

Fig. 6 Cartoon of the generation of the anti-kick in the head-on collision of two unequal-mass Schwarzschild black holes. Initially the smaller black hole moves faster and linear momentum is radiated mostly downwards, thus leading to an upwards recoil of the system [stage (1)]. At the merger the curvature is higher in the upper hemisphere of the distorted black hole (*cf.,* red-blue shading) and linear momentum is radiated mostly upwards leading to the anti-kick [stage (2)]. The black hole decelerates till a uniform curvature is restored on the horizon [stage (3)].

[7] I should remark that other explanations have also been suggested. One of them makes use of the Landau-Lifshitz pseudotensor and explains the recoil in terms of the cancellation of large and opposite fluxes of momentum, part of which are "swallowed" by the black hole [131]. Another one is even more essential and explains the antikick is in terms of the spectral features of the signal at large distances, quite independently of the presence of a black-hole horizon [132]. All of these views serve the scope of providing an intuitive description and are in my view equally valid and useful.

Although this picture refers to a head-on collision, it is supported by the findings in the CLA (where the direction of the ringdown kick is approximately opposite to that of the accumulated inspiral plus plunge kick) [127] and it can be generalized to a situation in which the black holes have different masses, different spins and are merging through an inspiral. Also in a more generic case, the newly-formed apparent horizon will have a complicated but globally anisotropic distribution of the curvature, determining the direction (which is in general varying in time) along which the gravitational waves will be emitted. Hence, the geometric properties in a dynamical horizon (of a black or white hole) determine its global dynamics. I next use the Robinson-Trautman spacetime to validate this picture.

4.2 A useful playground

The Robinson-Trautman spacetime represents a class of vacuum solutions admitting a congruence of null geodesics which are twist and shear-free [133], with a future stationary horizon and a dynamical past (outer trapping) horizon [134, 135, 136, 137, 138] (past apparent horizon hereafter). A Robinson-Trautman spacetime is thus regarded as an isolated nonspherical white hole emitting gravitational waves, where the evolution of the apparent horizon curvature-anisotropies and the total spacetime momentum dynamics can be related unambiguously. The metric is given by [139]

$$ds^2 = -\left(K - \frac{2M_\infty}{r} - \frac{2r\partial_u Q}{Q}\right) du^2 - 2dudr + \frac{r^2}{Q^2} d\Omega^2 \,, \tag{7}$$

where $Q = Q(u,\Omega)$, u is the standard null coordinate, r is the affine parameter of the outgoing null geodesics, and $\Omega = \{\theta,\phi\}$ are the angular coordinates on the unit sphere S^2. Here M_∞ is a constant and is related to the asymptotic mass, while the function $K(u,\Omega)$ is the Gaussian curvature of the surface corresponding to $r = 1$ and $u =$ constant, $K(u,\Omega) \equiv Q^2(1 + \nabla^2_\Omega \ln Q)$, where ∇^2_Ω is the Laplacian on S^2. The Einstein equations then lead to the evolution equation

$$\partial_u Q(u,\Omega) = -Q^3 \nabla^2_\Omega K(u,\Omega)/(12M_\infty) \,. \tag{8}$$

Any regular initial data $Q = Q(0,\Omega)$ will smoothly evolve according to (8) until it achieves a stationary configuration corresponding to a Schwarzschild black hole at rest or moving with a constant speed [140]. Equation (8) implies the existence of the constant of motion $\mathscr{A} \equiv \int_{S^2} d\Omega/Q^2$, which clearly represents the area of the surface $u =$ const., $r =$ const. and can be used to normalise Q so that $\mathscr{A} = 4\pi$. All the physically relevant information is contained in the function $Q(u,\Omega)$, and this includes the gravitational radiation, which can be extracted by relating $Q(u,\Omega)$ to the radiative part of the Riemann tensor [141, 142].

The past apparent horizon radius $R(u,\Omega)$ is given by the vanishing expansion of the future ingoing null geodesics, satisfying [134, 135]

$$Q^2\nabla^2_\Omega \ln R = K - 2M_\infty/R\,. \tag{9}$$

The mass and momentum of the black hole are computed at future null infinity using the Bondi four-momentum [139]

$$P^\alpha(u) \equiv \frac{M_\infty}{4\pi}\int_{S^2}\frac{\eta^\alpha}{Q^3}d\Omega\,, \tag{10}$$

with $(\eta^\alpha) = (1, \sin\theta\cos\phi, \sin\theta\sin\phi, \cos\theta)$. Given smooth initial data, the spacetime will evolve to a stationary non-radiative solution which, in axisymmetry, has the form $Q(\infty,\theta) = (1\mp vx)/\sqrt{1-v^2}$, with $x \equiv \cos\theta$ [139]. The Bondi four-momentum associated to $Q(\infty,\theta)$ has components

$$(P(\infty))^\alpha = \left(M_\infty/\sqrt{1-v^2}\right)(1,0,0,\pm v)\,, \tag{11}$$

so that the parameter v in $Q(\infty,\theta)$ can be interpreted as the velocity of the Schwarzschild black hole in the z-direction.

One of the difficulties with Robinson-Trautman spacetimes is the definition of physically meaningful initial data. Although this is meant more as a proof-of-principle than a realistic configuration, it is possible to adopt the prescription suggested in Ref. [142]

$$Q(0,\theta) = Q_0\left[\frac{1}{\sqrt{1-wx}} + \frac{q}{\sqrt{1+wx}}\right]^{-2}\,, \tag{12}$$

and which was interpreted to represent the final stages (*i.e.,* after a common apparent horizon is formed) of a head-on collision of two boosted black holes with opposite velocities w and mass ratio q [142]. In practice, to reproduce the situation shown in Fig. 6, it is sufficient to choose $w < 0$ and take $q \in [0,1]$; a more general class of initial data and the corresponding phenomenology can be found in [129, 143]. Note that Q_0 is chosen so that to $\mathscr{A} = 4\pi$ and that in general the deformed black hole will not be initially at rest. As a result, given the initial velocity $v_0 \equiv P^3(0)/P^0(0)$, a boost is performed transformation $\overline{P}^\alpha = \Lambda^\alpha_\beta(v_0)P^\beta$ so that $\overline{P}^3(0) = 0$ by construction. The numerical solution of eq. (8) with initial data (12) is performed using a Galerkin decomposition as discussed in detail in [139].

Figure 7 reports the typical evolution of a Robinson-Trautman spacetime with the lower panel showing the evolution of the curvature of the past apparent horizon $K_{\rm AH} \equiv 2M_\infty/R^3(x)$ at the north $(x=1)$ and south pole $(x=-1)$, and with the upper panel showing the evolution of the recoil velocity. Note that the two local curvatures are different initially, with the one in the upper hemisphere being larger than the one in the lower hemisphere (*cf.,* Fig. 6). However, as the gravitational radiation is emitted, this difference is erased. When this happens, the deceleration stops and the black hole attains its asymptotic recoil velocity. The inset reports the curvature difference relative to the asymptotic Schwarzschild one, $K_{\rm AH} - 1$, whose exponen-

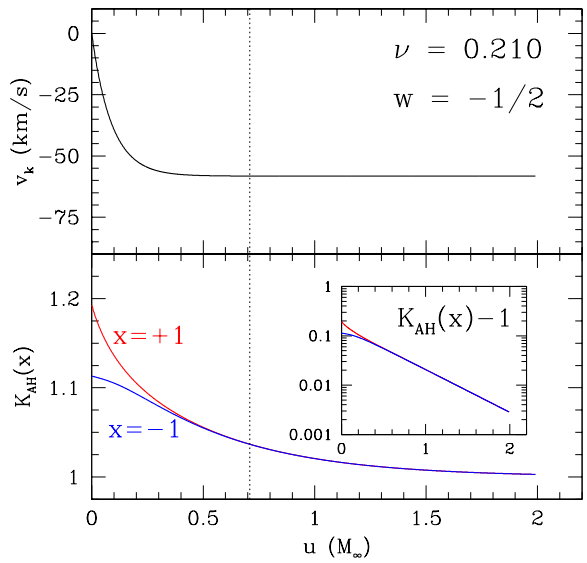

Fig. 7 Typical evolution of a Robinson-Trautman spacetime. Shown in the lower panel is the evolution of the curvature $K_{\rm AH}$ at the north ($x = 1$) and south pole ($x = -1$). Shown in the upper panel is the evolution of the recoil, which stops decreasing when the curvature difference is erased by the emitted radiation (dotted line). Note that the curvature decays exponentially to that of a Schwarzschild black hole (inset).

tially decaying behaviour is the one expected in a ringing black hole (see also Fig. 7 of Ref. [129]).

As mentioned before, the one shown in Fig. 7 is a typical evolution of a Robinson-Trautman spacetime and is not specific of the initial data (12). By varying the values of w, in fact, it is possible to increase or decreases the final recoil and a sign change in w simply inverts the curvature at the poles so that, for instance, initial data with $w > 0$ would yield a black hole accelerating in the positive z-direction. Interestingly, it is even possible to fine-tune the parameter w so that the recoil produced for a Robinson-Trautman spacetime mimics the anti-kick produced by the quasi-circular inspiral of nonspinning binaries. This is shown in Fig. 1, which reports the recoil as a function of the symmetric mass ratio $\nu \equiv q/(1+q)^2$, and where the dashed line refers to the anti-kick for the inspiral of nonspinning binaries in the CLA [127] (the parameters chosen, *i.e.,* $w = -0.425$ and $r_{12} = 2M$, are those minimising the differences). Considering that the two curves are related only logically and that the CLA one contains all the information about inspiralling black holes, including the orbital rotation, the match is surprisingly good.

It is also suggestive to think that the curve in Fig. 8 is actually composed of two different branches, one of which is characterized by large curvature gradients across the apparent horizon but small values of the curvature (this is the low-ν branch and is indicated with squares), while the other is characterized by small curvature gradients and large values of the curvature (this is the high-ν branch and is indicated

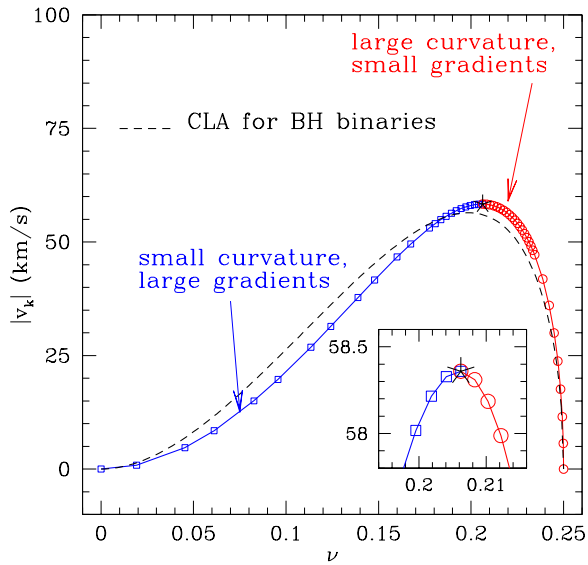

Fig. 8 Recoil velocity shown as a function of the symmetric mass ratio ν when $w = -0.425$, with the dashed line refers to the anti-kick from the inspiral of nonspinning binaries in the CLA [127]. Note that the curve can be thought as composed of two different branches.

with circles). The same recoil velocity can then be produced by two different values of ν, for which the effects of large curvature gradients and small local curvatures are the same as those produced by small curvature gradients but large local curvatures.

To go from this intuition to a mathematically well-defined measure one can compute the mass multipoles of the intrinsic curvature of the initial data using the formalism developed in [144] for dynamical horizons. Namely, it is possible to compute the mass moments as (the mass-current are obviously zero)

$$M_n \equiv \oint \frac{P_n(\tilde{x})}{Q^2(\theta)R(\theta)} d\Omega \,, \tag{13}$$

where $P_n(\tilde{x})$ is the Legendre polynomial in terms of the coordinate $\tilde{x}(\theta)$ which obeys $\partial_\theta \tilde{x} = -\sin\theta R(\theta)^2/(R_{\rm AH}^2 Q(\theta)^2)$, with $R_{\rm AH} \equiv \sqrt{\mathscr{A}_{\rm AH}/(4\pi)}$ and $\tilde{x}(0) = 1$. Using these multipoles it is possible to construct an effective-curvature parameter $K_{\rm eff}$ that represents a measure of the global curvature properties of the initial data and from which the recoil depends in an injective way. Because this effective-curvature parameter has to contain the contribution from the even and odd multipoles, the expression

$$K_{\rm eff} = M_2 |\sum_{n=1} M_{2n+1}/3^{n-1}| \,, \tag{14}$$

was found to reproduce exactly what expected (note $M_1 = 0$ to machine precision).

This is shown in Fig. 9, which reports the recoil velocity as a function of $K_{\rm eff}$. As predicted, and in contrast with Fig. 8, the relation between the curvature and the recoil is now injective, with the maximum recoil velocity being given by the maximum value of $K_{\rm eff}$ (see inset), and with the two branches coinciding. The expression (14) suggested above for $K_{\rm eff}$ is not unique and indeed a more generic one will have to include also the mass-current multipoles to account for the spin contributions (see discussion below). However, lacking a rigorous mathematical guidance, the phenomenological $K_{\rm eff}$ is a reasonable, intuitive approximation.

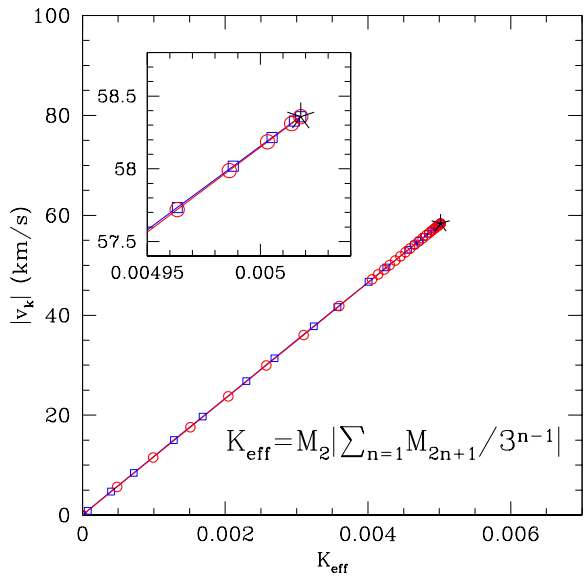

Fig. 9 Recoil velocity shown as a function of the effective curvature. In contrast with Fig. 8, which uses the same symbols employed here, the relation between the curvature and the recoil is now injective.

4.3 A more general view

Despite the valuable insight, the treatment summarised above and presented in Ref. [128] had obvious limitations. First, the Ansatz (14) for $K_{\rm eff}$, *i.e.,* $K_{\rm eff} = f_{\rm even}\,(M_{2\ell}) \times f_{\rm odd}\,(M_{2\ell+1})$ is not straightforwardly generalize to the non-axisymmetric case. Second, the functions $f_{\rm even}$ and $f_{\rm odd}$ can be written in the simplest possible form, *i.e.,* as a linear expansion in M_ℓ's, *i.e.,* $K_{\rm eff} = (a_2M_2 + a_4M_4 + \ldots) \times (a_3M_3 + a_5M_5 + \ldots)$, where the phenomenological coefficients a_ℓ's depend on the details of the employed initial data. Finally, the white-hole horizon analysis in

Robinson-Trautman spacetimes needs to be extended to the genuine black-hole horizon case.

While the focus in what discussed above (and presented in Ref. [128]) was on expressing the difference between the *final* kick velocity v_∞ and the instantaneous kick velocity $v_{\rm k}(u)$ at an (initial) given time u, in terms of the geometry of the common apparent horizon at that time u, it is possible to derive a more generic view based on geometric quantities that are evaluated at a given time during the evolution. More specifically, it is possible to consider the variation of the Bondi linear momentum vector in time $(dP_i^{\rm B}/du)(u)$ as the relevant geometric quantity to monitor at null infinity $\mathscr{J}^+$. This quantity can then be correlated with a counterpart on the black-hole horizon $\mathscr{H}^+$, *e.g.,* a vector $\tilde{K}^i_{\rm eff}(v)$ (function of an advanced time v), which represents an extension of the effective curvature introduced in the previous Section[8].

In the case of a Robinson-Trautman spacetime, the causal relation between the white-hole horizon $\mathscr{H}^-$ and null infinity $\mathscr{J}^+$ made possible to establish an explicit functional relation between $dv_{\rm k}/du$ and $K'_{\rm eff}(u)$. In the case of a generic black-hole horizon, such a direct causal relation between the inner horizon and $\mathscr{J}^+$ is lost. However, since the corresponding causal pasts of $\mathscr{J}^+$ and $\mathscr{H}^-$ coincide in part, non-trivial *correlations* are still possible and expected. These correlations can be measured by comparing geometric quantities $h_{\rm inn}(v)$ at $\mathscr{H}^+$ and $h_{\rm out}(u)$ at $\mathscr{J}^+$, both considered here as two timeseries[9]. In particular, it is reasonable to take $\tilde{K}^i_{\rm eff}(v)$ as $h_{\rm inn}(v)$ and $(dP_i^{\rm B}/du)(u)$ as $h_{\rm out}(u)$.

This approach resembles therefore the methodology adopted in *scattering* experiments. Gravitational dynamics in a given spacetime region affects the geometry of appropriately-chosen *outer* and *inner* hypersurfaces of the black-hole spacetime. These hypersurfaces are then understood as *test screens* on which suitable *geometric quantities* must be constructed. The correlations between the two encode geometric information about the dynamics in the bulk, providing information useful for an *inverse-scattering* approach to the near-horizon dynamics. In asymptotically flat black-hole spacetimes, null infinity $\mathscr{J}^+$ and the (event) black-hole horizon $\mathscr{H}^+$ provide natural choices for the outer and inner screens. This is summarised in the Carter-Penrose diagram in Fig. 10, which illustrates the cross-correlation approach to near-horizon gravitational dynamics. The event horizon $\mathscr{H}^+$ and null infinity $\mathscr{J}^+$ provide spacetime screens on which geometric quantities, accounting respectively for horizon deformations and wave emission, are measured. Their cross-correlation encodes information about the bulk spacetime dynamics.

The picture offered by Fig. 10 can be easily adapted to the 3+1 approach commonly adopted in numerical relativity. Since neither the black-hole event horizon nor null infinity are in general available during the evolution[10], it is possible to adopt as inner and outer screens a dynamical horizon $\mathscr{H}^+$ (future outer trapping

[8] Another appealing approach that has a similar goal of correlating strong-fields effects with (the visualization of) spacetime curvature has been proposed recently by the group in Caltech [145, 146].

[9] Note that the meaningful definition of timeseries cross-correlations requires the introduction of a (gauge-dependent) relation between advanced and retarded time coordinates v and u. In an initial value problem this is naturally provided by the 3+1 spacetime slicing by time t.

[10] The latter would properly require either characteristic or a hyperboloidal evolution approach.

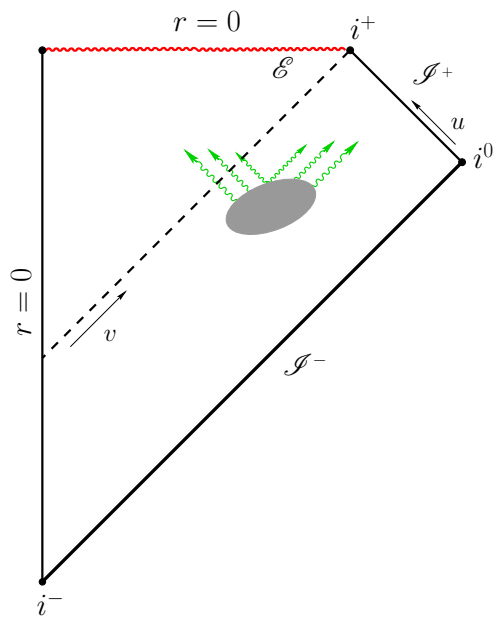

Fig. 10 Carter-Penrose diagram illustrating the *scattering* approach to near-horizon gravitational dynamics in a generic spherically symmetric collapse. The event horizon $\mathscr{H}^+$ and null infinity $\mathscr{I}^+$ provide spacetime canonical screens on which *geometric quantities*, respectively accounting for horizon deformations and wave emission, are defined. Their cross-correlation encodes nontrivially information about the bulk spacetime dynamics.

horizon [147, 148, 149]) and a timelike tube $\mathscr{B}$ at large spatial distances, respectively. In this case, the time function t associated with the 3+1 spacetime slicing provides a (gauge) mapping between the retarded and advanced times u and v, so that cross-correlations between geometric quantities at $\mathscr{H}^+$ and $\mathscr{B}$ can be calculated as standard timeseries $h_{\rm inn}(t)$ and $h_{\rm out}(t)$. This is summarised in the Carter-Penrose diagram in Fig. 11, which is the same as in Fig. 10, but where the 3+1 slicing sets an in-built common time t for cross-correlations between the dynamical horizon $\mathscr{H}^+$ (*i.e.,* the inner screen) and a large-distance timelike hypersurface $\mathscr{B}$ (*i.e.,* the outer screen).

Within this conceptual framework it is then possible to define a phenomenological curvature vector $\tilde{K}_i^{\rm eff}(t)$ in terms of the mass multipoles of the Ricci scalar curvature ${}^2R$ at $\mathscr{H}^+$ and show that this is closely correlated with a geometric quantities $(dP_i^{\mathscr{B}}/dt)(t)$, representing the variation of the Bondi linear momentum time on $\mathscr{I}^+$. How to do this in practice for a black-hole spacetime requires much more space that I can take in this contribution and therefore refer the interested reader to Refs. [129, 130], where this is discussed in great detail.

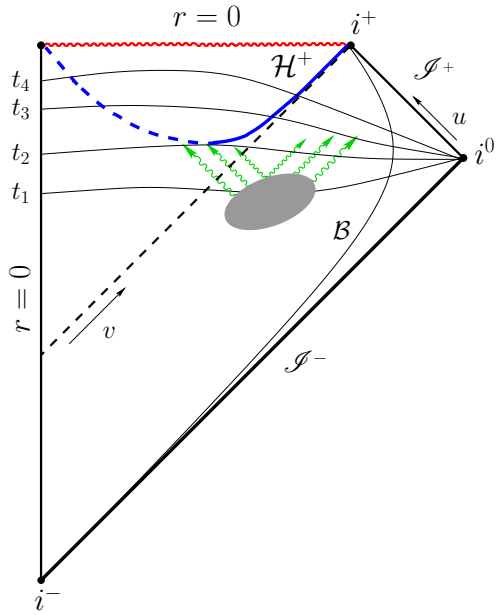

Fig. 11 Carter-Penrose diagram for the *scattering* picture in a Cauchy initial value approach. The dynamical horizon $\mathscr{H}^+$ and a large-distance timelike hypersurface $\mathscr{B}$ provide inner and outer screens. Note that the dynamical horizon is split in two portions: outer and inner (solid and dashed blue lines, respectively) and that the 3+1 slicing sets a common time t for cross-correlations.

4.4 Summary

The discussion reported above demonstrates that qualitative aspects of the post-merger recoil dynamics at infinity can be understood in terms of the evolution of the geometry of the common horizon of the resulting black hole. Moreover, suitably-built quantities defined on inner and outer worldtubes (represented either by dynamical horizons or by timelike boundaries) can act as test screens responding to the spacetime geometry in the bulk, thus opening the way to a cross-correlation approach to probe the dynamics of spacetime. This picture was shown to hold both for a simple Robinson-Trautman spacetime, but also for more generic binary black-hole spacetimes. In this latter case, this is possible through the construction of a phenomenological vector $\tilde{K}_i^{\rm eff}(t)$ from the Ricci curvature scalar ${}^2R$ on the dynamical horizon sections, which then captures the global properties of the flux of Bondi linear momentum $(dP_i^{\rm B}/dt)(t)$ at infinity, namely the acceleration of the BH.

A geometric framework looking at the horizon's properties offers a number of connections with the literature developing around the use of horizons to study the dynamics of black holes, as well as with the interpretations of such dynamics in terms of a viscous-hydrodynamics analogy. Much of the machinery developed using dynamical trapping horizons as inner screens can be extended also when a common horizon is not formed (as in the calculations reported in Ref. [150]). While in such

cases the identification of an appropriate hypersurface for the inner screen can be more difficult, once this is found its geometrical properties can be used along the lines of the cross-correlation approach discussed here for dynamical horizons.

5 Conclusions

The "three little piece" for numerical computer and relativity presented in the sections above ought to provide a reasonable idea of the "Renaissance" that numerical relativity is now experiencing. More importantly, they should be able to convey the enormous potential that numerical-relativity simulations have in revealing aspects of the theory that cannot be handled analytically, or in exploring nonlinear regimes that cannot be investigated through perturbative approaches. As remarked repeatedly, the examples brought represent only a personal (and biased) selection of the intense work carried out recently and surely are not exhaustive in terms of the physical scenarios that can be explored. Much more can be said about this and surely it will not have to wait for the bicentenary of Einstein's stay in Prague.

Acknowledgements

The work discussed here has been carried out in collaboration with M. A. Aloy, L. Baiotti, B. Giacomazzo, J. Granot, J. L. Jaramillo, C. Kouveliotou, R. P. Macedo K. Takami, whom I am indebted with. My thanks go also to the numerical-relativity group of the AEI for providing such a stimulating and productive environment. Support comes through the DFG grant SFB/Trans-regio 7 and "CompStar", a Research Networking Programme of the ESF. The calculations have been performed on the clusters at the AEI.

References

1. F. Pretorius, *Evolution of binary black hole spacetimes*, Phys. Rev. Lett. **95**, 121101 (2005)
2. M. Campanelli, C.O. Lousto, P. Marronetti, Y. Zlochower, *Accurate evolutions of orbiting black-hole binaries without excision*, Phys. Rev. Lett. **96**, 111101 (2006)
3. J.G. Baker, J. Centrella, D.I. Choi, M. Koppitz, J. van Meter, *Gravitational wave extraction from an inspiraling configuration of merging black holes*, Phys. Rev. Lett. **96**, 111102 (2006)
4. L. Baiotti, L. Rezzolla, *Challenging the paradigm of singularity excision in gravitational collapse*, Phys. Rev. Lett. **97**, 141101 (2006)
5. T. Chu, H.P. Pfeiffer, M.A. Scheel, *High accuracy simulations of black hole binaries: Spins anti-aligned with the orbital angular momentum*, Phys. Rev. D **80**(12), 124051 (2009)
6. L. Baiotti, B. Giacomazzo, L. Rezzolla, *Accurate evolutions of inspiralling neutron-star binaries: Prompt and delayed collapse to a black hole*, Phys. Rev. D **78**(8), 084033 (2008)
7. J. Centrella, J.G. Baker, B.J. Kelly, J.R. van Meter, *Black-hole binaries, gravitational waves, and numerical relativity*, Reviews of Modern Physics **82**, 3069 (2010)

8. H.P. Pfeiffer, *Numerical simulations of compact object binaries*, Classical and Quantum Gravity **29**(12), 124004 (2012)
9. D. Radice, L. Rezzolla, *Discontinuous Galerkin methods for general-relativistic hydrodynamics: Formulation and application to spherically symmetric spacetimes*, Phys. Rev. D **84**(2), 024010 (2011)
10. D. Radice, L. Rezzolla, *THC: a new high-order finite-difference high-resolution shock-capturing code for special-relativistic hydrodynamics*, Astronomy and Astrophysics **547**, A26 (2012)
11. T. Nakamura, K. Oohara, Y. Kojima, *General relativistic collapse to black holes and gravitational waves from black holes*, Prog. Theor. Phys. Suppl. **90**, 1 (1987)
12. C. Bona, J. Massó, E. Seidel, J. Stela, *New formalism for numerical relativity*, Phys. Rev. Lett. **75**, 600 (1995)
13. M. Shibata, T. Nakamura, *Evolution of three-dimensional gravitational waves: Harmonic slicing case*, Phys. Rev. D **52**, 5428 (1995)
14. T.W. Baumgarte, S.L. Shapiro, *On the numerical integration of Einstein's field equations*, Phys. Rev. D **59**, 024007 (1999)
15. M. Alcubierre, B. Brügmann, P. Diener, et al., *Gauge conditions for long-term numerical black hole evolutions without excision*, Phys. Rev. D **67**, 084023 (2003)
16. F. Pretorius, *Numerical relativity using a generalized harmonic decomposition*, Classical Quantum Gravity **22**, 425 (2005)
17. D. Alic, C. Bona, C. Bona-Casas, *Towards a gauge-polyvalent numerical relativity code*, Phys. Rev. D **79**(4), 044026 (2009)
18. S. Bernuzzi, D. Hilditch, *Constraint violation in free evolution schemes: comparing BSSNOK with a conformal decomposition of Z4*, Phys. Rev. D **81**, 084003 (2010)
19. D. Müller, J. Grigsby, B. Brügmann, *Dynamical shift condition for unequal mass black hole binaries*, Phys. Rev. D **82**, 064004 (2010)
20. E. Schnetter, *Time step size limitation introduced by the BSSN Gamma driver*, Class. Quant. Grav. **27**, 167001 (2010)
21. D. Alic, C. Bona-Casas, C. Bona, L. Rezzolla, C. Palenzuela, *Conformal and covariant formulation of the Z4 system with constraint-violation damping*, Phys. Rev. D **85**, 064040 (2012)
22. M. Shibata, K. Taniguchi, *Merger of binary neutron stars to a black hole: Disk mass, short gamma-ray bursts, and quasinormal mode ringing*, Phys. Rev. D **73**, 064027 (2006)
23. M. Anderson, E.W. Hirschmann, L. Lehner, et al., *Magnetized neutron star mergers and gravitational wave signals*, Phys. Rev. Lett. **100**, 191101 (2008)
24. Y.T. Liu, S.L. Shapiro, Z.B. Etienne, K. Taniguchi, *General relativistic simulations of magnetized binary neutron star mergers*, Phys. Rev. D **78**, 024012 (2008)
25. B. Giacomazzo, L. Rezzolla, L. Baiotti, *Can magnetic fields be detected during the inspiral of binary neutron stars?*, Mon. Not. R. Astron. Soc. **399**, L164 (2009)
26. B. Giacomazzo, L. Rezzolla, N. Stergioulas, *Collapse of differentially rotating neutron stars and cosmic censorship*, Phys. Rev. D **84**(2), 024022 (2011)
27. L. Rezzolla, L. Baiotti, B. Giacomazzo, D. Link, J.A. Font, *Accurate evolutions of unequal-mass neutron-star binaries: properties of the torus and short GRB engines*, Classical Quantum Gravity **27**(11), 114105 (2010)
28. K. Kiuchi, Y. Sekiguchi, M. Shibata, K. Taniguchi, *Exploring binary-neutron-star-merger scenario of short-gamma-ray bursts by gravitational-wave observation*, Phys. Rev. Lett. **104**(14), 141101 (2010)
29. L. Baiotti, T. Damour, B. Giacomazzo, A. Nagar, L. Rezzolla, *Analytic modelling of tidal effects in the relativistic inspiral of binary neutron stars*, Phys. Rev. Lett. **105**, 261101 (2010)
30. S. Bernuzzi, A. Nagar, M. Thierfelder, B. Brügmann, *Tidal effects in binary neutron star coalescence*, Phys. Rev. D **86**(4), 044030 (2012)
31. K. Hotokezaka, K. Kyutoku, M. Shibata, *Exploring tidal effects of coalescing binary neutron stars in numerical relativity*, Phys. Rev. D **87**(4), 044001 (2013)
32. J. Abadie, B.P. Abbott, R. Abbott, et al., *Topical review: Predictions for the rates of compact binary coalescences observable by ground-based gravitational-wave detectors*, Classical Quantum Gravity **27**(17), 173001 (2010)

33. B. Paczynski, *Gamma-ray bursters at cosmological distances*, Astrophys. J. Lett. **308**, L43 (1986)
34. D. Eichler, M. Livio, T. Piran, D.N. Schramm, *Nucleosynthesis, neutrino bursts and gamma-rays from coalescing neutron stars*, Nature **340**, 126 (1989)
35. R. Narayan, B. Paczynski, T. Piran, *Gamma-ray bursts as the death throes of massive binary stars*, Astrophys. J. **395**, L83 (1992)
36. M. Ruffert, H.T. Janka, *Gamma-ray bursts from accreting black holes in neutron star mergers*, Astron. Astrophys. **344**, 573 (1999)
37. S. Rosswog, E. Ramirez-Ruiz, M.B. Davies, *High-resolution calculations of merging neutron stars - III. Gamma-ray bursts*, Mon. Not. R. Astron. Soc. **345**, 1077 (2003)
38. E. Nakar, *Short-hard gamma-ray bursts*, Phys. Rep. **442**, 166 (2007)
39. W.H. Lee, E. Ramirez-Ruiz, *The progenitors of short gamma-ray bursts*, New J. Phys. **9**, 17 (2007)
40. D.B. Fox, D.A. Frail, P.A. Price, et al., *The afterglow of GRB050709 and the nature of the short-hard gamma-ray bursts*, Nature **437**, 845 (2005)
41. J.X. Prochaska, J.S. Bloom, H.W. Chen, et al., *The galaxy hosts and large-scale environments of short-hard gamma-ray bursts*, Astrophys. J. **642**, 989 (2006)
42. L. Rezzolla, B. Giacomazzo, L. Baiotti, et al., *The missing link: Merging neutron stars naturally produce jet-like structures and can power short Gamma-Ray Bursts*, Astrophys. J. **732**(11), L6 (2011)
43. B. Giacomazzo, L. Rezzolla, *WhiskyMHD: a new numerical code for general relativistic magnetohydrodynamics*, Classical Quantum Gravity **24**, S235 (2007)
44. D. Pollney, C. Reisswig, L. Rezzolla, et al., *Recoil velocities from equal-mass binary black-hole mergers: a systematic investigation of spin-orbit aligned configurations*, Phys. Rev. D **76**, 124002 (2007)
45. L. Baiotti, I. Hawke, P. Montero, L. Rezzolla, *A new three-dimensional general-relativistic hydrodynamics code*, in *Computational Astrophysics in Italy: Methods and Tools*, vol. 1, ed. by R. Capuzzo-Dolcetta (MSAIt, Trieste, 2003), p. 210
46. L. Baiotti, I. Hawke, P.J. Montero, et al., *Three-dimensional relativistic simulations of rotating neutron star collapse to a Kerr black hole*, Phys. Rev. D **71**, 024035 (2005)
47. L. Antón, O. Zanotti, J.A. Miralles, et al., *Numerical 3+1 general relativistic magnetohydrodynamics: a local characteristic approach*, Astrophys. J. **637**, 296 (2006)
48. G. Toth, *The* div $B = 0$ *constraint in shock-capturing magnetohydrodynamics codes*, J. Comput. Phys. **161**, 605 (2000)
49. E. Schnetter, S.H. Hawley, I. Hawke, *Evolutions in 3D numerical relativity using fixed mesh refinement*, Classical Quantum Gravity **21**(6), 1465 (2004)
50. C. Kouveliotou, C.A. Meegan, G.J. Fishman, et al., *Identification of two classes of gamma-ray bursts*, Astrophys. J. **413**, L101 (1993)
51. L. Dessart, C.D. Ott, A. Burrows, S. Rosswog, E. Livne, *Neutrino signatures and the neutrino-driven wind in binary neutron star mergers*, Astrophys. J. **690**, 1681 (2009)
52. S. Setiawan, M. Ruffert, H. Janka, *Non-stationary hyperaccretion of stellar-mass black holes in three dimensions: torus evolution and neutrino emission*, Mon. Not. R. Astron. Soc. **352**, 753 (2004)
53. J.C. McKinney, D.A. Uzdensky, *A reconnection switch to trigger gamma-ray burst jet dissipation*, Mon. Not. R. Astron. Soc. **419**, 573 (2012)
54. R.H. Price, S. Rosswog, *Producing ultrastrong magnetic fields in neutron star mergers*, Science **312**, 719 (2006)
55. M.A. Aloy, H. Janka, E. Müller, *Relativistic outflows from remnants of compact object mergers and their viability for short gamma-ray bursts*, Astronomy and Astrophysics **436**, 273 (2005)
56. S.S. Komissarov, N. Vlahakis, A. Königl, M.V. Barkov, *Magnetic acceleration of ultrarelativistic jets in gamma-ray burst sources*, Mon. Not. R. Astron. Soc. **394**, 1182 (2009)
57. S.A. Balbus, J.F. Hawley, *Instability, turbulence, and enhanced transport in accretion disks*, Reviews of Modern Physics **70**, 1 (1998)

58. D.M. Siegel, R. Ciolfi, A.I. Harte, L. Rezzolla, *On the magnetorotational instability in relativistic hypermassive neutron stars*, ArXiv e-prints [arXiv:1302.4368 [gr-qc]] (2013)
59. B. Giacomazzo, L. Rezzolla, L. Baiotti, *Accurate evolutions of inspiralling and magnetized neutron stars: Equal-mass binaries*, Phys. Rev. D **83**(4), 044014 (2011)
60. M. Obergaulinger, P. Cerdá-Durán, E. Müller, M.A. Aloy, *Semi-global simulations of the magneto-rotational instability in core collapse supernovae*, Astronomy and Astrophysics **498**, 241 (2009)
61. R.D. Blandford, R.L. Znajek, *Electromagnetic extraction of energy from Kerr black holes*, Mon. Not. R. Astron. Soc. **179**, 433 (1977)
62. S.S. Komissarov, M.V. Barkov, *Activation of the Blandford-Znajek mechanism in collapsing stars*, Mon. Not. R. Astron. Soc. **397**, 1153 (2009)
63. D. Radice, L. Rezzolla, *Universality and intermittency in relativistic turbulent flows of a hot plasma*, Astrophys. J. **766**, L10 (2013)
64. J. Zrake, A.I. MacFadyen, *Spectral and intermittency properties of relativistic turbulence*, Astrophys. J. **763**, L12 (2013)
65. Z.B. Etienne, V. Paschalidis, S.L. Shapiro, *General-relativistic simulations of black-hole-neutron-star mergers: Effects of tilted magnetic fields*, Phys. Rev. D **86**(8), 084026 (2012)
66. G. Lesur, G.I. Ogilvie, *Localized magnetorotational instability and its role in the accretion disc dynamo*, Mon. Not. R. Astron. Soc. **391**, 1437 (2008)
67. M.A. Aloy, L. Rezzolla, *A powerful hydrodynamic booster for relativistic jets*, Astrophys. J. **640**, L115 (2006)
68. J. Granot, S.S. Komissarov, A. Spitkovsky, *Impulsive acceleration of strongly magnetized relativistic flows*, Mon. Not. R. Astron. Soc. **411**, 1323 (2011)
69. K. Dionysopoulou, D. Alic, C. Palenzuela, L. Rezzolla, B. Giacomazzo, *General-relativistic resistive magnetohydrodynamics in three dimensions: formulation and tests*, ArXiv e-prints [arXiv:1208.3487 [gr-qc]] (2012)
70. J.S. Bloom, J.X. Prochaska, D. Pooley, et al., *Closing in on a short-hard burst progenitor: Constraints from early-time optical imaging and spectroscopy of a possible host galaxy of GRB 050509b*, Astrophys. J. **638**, 354 (2006)
71. M. Ackermann, K. Asano, W.B. Atwood, et al., *Fermi observations of GRB 090510: A short-hard gamma-ray burst with an additional, hard power-law component from 10 keV TO GeV energies*, Astrophys. J. **716**, 1178 (2010)
72. R. Oechslin, H.T. Janka, *Torus formation in neutron star mergers and well-localized short gamma-ray burst*, Mon. Not. R. Astron. Soc. **368**, 1489 (2006)
73. R. Birkl, M.A. Aloy, H.T. Janka, E. Müller, *Neutrino pair annihilation near accreting, stellar-mass black holes*, Astron. Astrophys. **463**, 51 (2007)
74. H.K. Lee, R.A.M.J. Wijers, G.E. Brown, *The Blandford-Znajek process as a central engine for a gamma-ray burst*, Physics Reports **325**, 83 (2000)
75. J. Granot, A. Königl, T. Piran, *Implications of the early X-ray afterglow light curves of Swift gamma-ray bursts*, Mon. Not. R. Astron. Soc. **370**, 1946 (2006)
76. A.A. Abdo, M. Ackermann, K. Asano, et al., *Fermi observations of high-energy gamma-ray emission from GRB 080825C*, Astrophys. J. **707**, 580 (2009)
77. J. Granot, J. Cohen-Tanugi, E. do Couto e Silva, *Opacity buildup in impulsive relativistic sources*, Astrophys. J. **677**, 92 (2008)
78. M. De Pasquale, P. Schady, N.P.M. Kuin, et al., *Swift and Fermi observations of the early afterglow of the short gamma-ray burst 090510*, Astrophys. J. **709**, L146 (2010)
79. E. Rossi, D. Lazzati, M.J. Rees, *Afterglow light curves, viewing angle and the jet structure of γ-ray bursts*, Mon. Not. R. Astron. Soc. **332**, 945 (2002)
80. F. Peng, A. Königl, J. Granot, *Two-component jet models of gamma-ray burst sources*, Astrophys. J. **626**, 966 (2005)
81. R.M. Wald, *General relativity* (The University of Chicago Press, Chicago, 1984)
82. K. Thorne, *Nonspherical gravitational collapse: A short review*, in *Magic Without Magic: John Archibald Wheeler*, ed. by J. Klauder (Freeman, San Francisco, 1972), p. 231
83. J.M.M. Senovilla, *A reformulation of the hoop conjecture*, Europhysics Letters **81**, 20004 (2008)

84. P.C. Argyres, S. Dimopoulos, J. March-Russell, *Black holes and sub-millimeter dimensions*, Physics Letters B **441**, 96 (1998)
85. H. Yoshino, Y. Nambu, *Black hole formation in the grazing collision of high-energy particles*, Phys. Rev. D **67**(2), 024009 (2003)
86. C.M. Yoo, H. Ishihara, M. Kimura, S. Tanzawa, *Hoop conjecture and the horizon formation cross section in Kaluza-Klein spacetimes*, Phys. Rev. D **81**(2), 024020 (2010)
87. S. Dimopoulos, G. Landsberg, *Black holes at the Large Hadron Collider*, Phys. Rev. Lett. **87**(16), 161602 (2001)
88. U. Sperhake, V. Cardoso, F. Pretorius, E. Berti, J.A. Gonzalez, *The high-energy collision of two black holes*, Phys. Rev. Lett. **101**, 161101 (2008)
89. M. Shibata, H. Okawa, T. Yamamoto, *High-velocity collision of two black holes*, Phys. Rev. D **78**(10), 101501 (2008)
90. U. Sperhake, V. Cardoso, F. Pretorius, et al., *Cross section, final spin, and zoom-whirl behavior in high-energy black-hole collisions*, Physical Review Letters **103**(13), 131102 (2009)
91. D.M. Eardley, S.B. Giddings, *Classical black hole production in high-energy collisions*, Phys. Rev. D **66**(4), 044011 (2002)
92. P.D. D'eath, P.N. Payne, *Gravitational radiation in black-hole collisions at the speed of light. I. Perturbation treatment of the axisymmetric collision*, Phys. Rev. D **46**, 658 (1992)
93. P.D. D'eath, P.N. Payne, *Gravitational radiation in black-hole collisions at the speed of light. II. Reduction to two independent variables and calculation of the second-order news function*, Phys. Rev. D **46**, 675 (1992)
94. P.D. D'eath, P.N. Payne, *Gravitational radiation in black-hole collisions at the speed of light. III. Results and conclusions*, Phys. Rev. D **46**, 694 (1992)
95. M.W. Choptuik, F. Pretorius, *Ultrarelativistic Particle Collisions*, Phys. Rev. Lett. **104**(11), 111101 (2010)
96. L. Rezzolla, K. Takami, *Black-hole production from ultrarelativistic collisions*, Classical and Quantum Gravity **30**(1), 012001 (2013)
97. W.E. East, F. Pretorius, *Ultrarelativistic black hole formation*, ArXiv e-prints [arXiv:1210.0443 [gr-qc]] (2012)
98. D.H. Rischke, S. Bernard, J.A. Maruhn, *Relativistic hydrodynamics for heavy-ion collisions. I. General aspects and expansion into vacuum*, Nuclear Physics A **595**, 346 (1995)
99. T. Kellerman, L. Rezzolla, D. Radice, *Critical phenomena in neutron stars: II. Head-on collisions*, Classical Quantum Gravity **27**(23), 235016 (2010)
100. T. Kellerman, L. Baiotti, B. Giacomazzo, L. Rezzolla, *An improved formulation of the relativistic hydrodynamics equations in 2D Cartesian coordinates*, Classical Quantum Gravity **25**(22), 225007 (2008)
101. D. Radice, L. Rezzolla, T. Kellerman, *Critical phenomena in neutron stars: I. Linearly unstable nonrotating models*, Classical Quantum Gravity **27**(23), 235015 (2010)
102. J.D. Bjorken, *Highly relativistic nucleus-nucleus collisions: The central rapidity region*, Phys. Rev. D **27**, 140 (1983)
103. P. Huovinen, P.V. Ruuskanen, *Hydrodynamic models for heavy ion collisions*, Annual Review of Nuclear and Particle Science **56**, 163 (2006)
104. K.J. Jin, W.M. Suen, et al., *Critical phenomena in head-on collision of neutron stars*, Phys. Rev. Lett **98**, 131101 (2007)
105. M.B. Wan, *Universality and properties of neutron star type I critical collapses*, Classical and Quantum Gravity **28**(15), 155002 (2011)
106. R.D. Heuer, *News from CERN, LHC status and strategy for linear colliders*, ArXiv e-prints [arXiv:1202.5860 [physics.acc-ph]] (2012)
107. P. Blasi, *On the origin of very high energy cosmic rays*, Mod. Phys. Lett. **A20**, 3055 (2005)
108. A. Peres, *Classical radiation recoil*, Phys. Rev. **128**, 2471 (1962)
109. M.J. Fitchett, S. Detweiler, *Linear momentum and gravitational waves – Circular orbits around a Schwarzschild black hole*, Mon. Not. R. Astron. Soc. **211**, 933 (1984)
110. A.G. Wiseman, *Coalescing binary systems of compact objects to (post)5/2 Newtonian order. 2. Higher order wave forms and radiation recoil*, Phys. Rev. D **46**, 1517 (1992)

111. Z. Andrade, R.H. Price, *Head-on collisions of unequal mass black holes: Close-limit predictions*, Phys. Rev. D **56**, 6336 (1997)
112. J.G. Baker, J. Centrella, D.I. Choi, et al., *Getting a kick out of numerical relativity*, Astrophys. J. **653**, L93 (2006)
113. J.A. Gonzalez, U. Sperhake, B. Bruegmann, M. Hannam, S. Husa, *Total recoil: the maximum kick from nonspinning black-hole binary inspiral*, Phys. Rev. Lett. **98**, 091101 (2007)
114. M. Campanelli, C.O. Lousto, Y. Zlochower, D. Merritt, *Maximum gravitational recoil*, Phys. Rev. Lett. **98**, 231102 (2007)
115. F. Herrmann, I. Hinder, D. Shoemaker, P. Laguna, R.A. Matzner, *Gravitational recoil from spinning binary black hole mergers*, Astrophys. J. **661**, 430 (2007)
116. M. Koppitz, al., *Recoil Velocities from Equal-Mass Binary-Black-Hole Mergers*, Phys. Rev. Lett. **99**, 041102 (2007)
117. C.O. Lousto, Y. Zlochower, *Further insight into gravitational recoil*, Phys. Rev. D **77**, 044028 (2008)
118. D. Pollney, et al., *Recoil velocities from equal-mass binary black-hole mergers: a systematic investigation of spin-orbit aligned configurations*, Phys. Rev. D **76**, 124002 (2007)
119. J. Healy, et al., *Superkicks in hyperbolic encounters of binary black holes*, Phys. Rev. Lett. **102**, 041101 (2009)
120. C.O. Lousto, Y. Zlochower, *Hangup kicks: still larger recoils by partial spin-orbit alignment of black-hole binaries*, Physical Review Letters **107**(23), 231102 (2011)
121. M. Campanelli, C.O. Lousto, Y. Zlochower, D. Merritt, *Large merger recoils and spin flips from generic black-hole binaries*, Astrophys. J. **659**, L5 (2007)
122. J.A. Gonzalez, M.D. Hannam, U. Sperhake, B. Bruegmann, S. Husa, *Supermassive kicks for spinning black holes*, Phys. Rev. Lett. **98**, 231101 (2007)
123. L. Rezzolla, *Modelling the final state from binary black-hole coalescences*, Class. Quant. Grav. **26**, 094023 (2009)
124. C.O. Lousto, Y. Zlochower, *Nonlinear gravitational recoil from the mergers of precessing black-hole binaries*, ArXiv e-prints [arXiv:1211.7099 [gr-qc]] (2012)
125. J.D. Schnittman, A. Buonanno, J.R. van Meter, et al., *Anatomy of the binary black hole recoil: A multipolar analysis*, Phys. Rev. D **77**(4), 044031 (2008)
126. Y. Mino, J. Brink, *Gravitational radiation from plunging orbits – Perturbative study*, Phys. Rev. D **78**, 124015 (2008)
127. A. Le Tiec, L. Blanchet, C.M. Will, *Gravitational-wave recoil from the ringdown phase of coalescing black hole binaries*, Class. Quant. Grav. **27**, 012001 (2010)
128. L. Rezzolla, R.P. Macedo, J.L. Jaramillo, *Understanding the 'anti-kick' in the merger of binary black holes*, Phys. Rev. Lett. **104**, 221101 (2010)
129. J.L. Jaramillo, R.P. Macedo, P. Moesta, L. Rezzolla, *Black-hole horizons as probes of black-hole dynamics. I. Post-merger recoil in head-on collisions*, Phys. Rev. D **85**, 084030 (2012)
130. J.L. Jaramillo, R.P. Macedo, P. Moesta, L. Rezzolla, *Black-hole horizons as probes of black-hole dynamics. II. Geometrical insights*, Phys. Rev. D **85**, 084031 (2012)
131. G. Lovelace, et al., *Momentum flow in black-hole binaries: II. Numerical simulations of equal-mass, head-on mergers with antiparallel spins*, Phys. Rev. D **82**, 064031 (2010)
132. R.H. Price, G. Khanna, S.A. Hughes, *Systematics of black hole binary inspiral kicks and the slowness approximation*, Phys. Rev. D **83**(12), 124002 (2011)
133. I. Robinson, A. Trautman, *Some spherical gravitational waves in general relativity*, Proc. Roy. Soc. Lond. **A265**, 463 (1962)
134. R. Penrose, *Naked singularities*, Ann. N.Y. Acad. Sci. **224**, 125 (1973)
135. K.P. Tod, *Analogue of the past horizon in the Robinson-Trautman metrics*, Class. Quant. Grav. **6**, 1159 (1989)
136. E.W.M. Chow, A.W.C. Lun, *Apparent horizons in vacuum Robinson-Trautman space-times*, J. Austral. Math. Soc. Serv. B **41**, 217 (1999)
137. W. Natorf, J. Tafel, *Horizons in Robinson-Trautman space-times*, Class. Quant. Grav. **25**, 195012 (2008)
138. J. Podolsky, O. Svitek, *Past horizons in Robinson-Trautman spacetimes with a cosmological constant*, Phys. Rev. D **80**, 124042 (2009)

139. R.P. Macedo, A. Saa, *Gravitational wave recoil in Robinson-Trautman spacetimes*, Phys. Rev. D **78**, 104025 (2008)
140. P.T. Chrusciel, *Semi-global existence and convergence of solutions of the Robinson-Trautman (2-dimensional Calabi) equation*, Commun. Math. Phys. **137**, 289 (1991)
141. H.P. de Oliveira, I. Damiao Soares, *Gravitational wave emission from a bounded source: The nonlinear regime*, Phys. Rev. D **70**, 084041 (2004)
142. R.F. Aranha, H.P. de Oliveira, I. Damiao Soares, E.V. Tonini, *The efficiency of gravitational bremsstrahlung production in the collision of two Schwarzschild black holes*, Int. J. Mod. Phys. D **17**, 2049 (2008)
143. R.F. Aranha, I.D. Soares, E.V. Tonini, *Mass-energy and momentum extraction by gravitational wave emission in the merger of two colliding black holes: The non-head-on case*, Phys. Rev. D **85**(2), 024003 (2012)
144. A. Ashtekar, J. Engle, T. Pawlowski, C. Van Den Broeck, *Multipole Moments of Isolated Horizons*, Classical Quantum Gravity **21**, 2549 (2004)
145. R. Owen, J. Brink, Y. Chen, et al., *Frame-dragging vortexes and tidal tendexes attached to colliding black holes: visualizing the curvature of spacetime*, Phys. Rev. Lett. **106**(15), 151101 (2011)
146. D.A. Nichols, R. Owen, F. Zhang, et al., *Visualizing spacetime curvature via frame-drag vortexes and tidal tendexes: General theory and weak-gravity applications*, Phys. Rev. D **84**, 124014 (2011)
147. S.A. Hayward, *General laws of black hole dynamics*, Phys. Rev. D **49**(12), 6467 (1994)
148. A. Ashtekar, B. Krishnan, *Dynamical horizons and their properties*, Phys. Rev. D **68**, 104030 (2003)
149. A. Ashtekar, B. Krishnan, *Isolated and dynamical horizons and their applications*, Living Rev. Relativ. **7**, 10 (2004)
150. U. Sperhake, E. Berti, V. Cardoso, F. Pretorius, N. Yunes, *Superkicks in ultrarelativistic encounters of spinning black holes*, Phys. Rev. D **83**, 024037 (2011)